Ore Geology Reviews 145 (2022) 104875

Contents lists available at ScienceDirect

Ore Geology Reviews

journal homepage: www.elsevier.com/locate/oregeorev

Polymetallic nanoparticles in pyrite from massive and stockwork ores of VMS deposits of the Iberian Pyrite Belt

José M. González-Jiménez [a,*,1], Lola Yesares [b], Rubén Piña [b], Reinaldo Sáez [c], Gabriel Ruiz de Almodóvar [c], Fernando Nieto [a,d], Sergio Tenorio [e]

[a] Instituto Andaluz de Ciencias de la Tierra, CSIC-Universidad de Granada, Avda. de las Palmeras 4, 18100 Armilla, Granada, Spain
[b] Departamento de Mineralogía y Petrología, Facultad de Ciencias Geológicas, Universidad Complutense de Madrid, C/ José Antonio Novais, 2, 28040 Madrid, Spain
[c] Departamento de Ciencias de la Tierra, Universidad de Huelva, Av. 3 de Marzo s/n, 21071 Huelva, Spain
[d] Departamento de Mineralogía y Petrología, Facultad de Ciencias, Universidad de Granada, Avda. Fuentenueva s/n, 18002 Granada, Spain
[e] Tharsis Mining, Pueblo Nuevo, s/n, Tharsis-Alosno, Huelva, Spain

ARTICLE INFO

Keywords:
Trace metals
Gold
Arsenian pyrite
volcanogenic massive sulfides (VMS)
Iberian Pyrite Belt (IPB)

ABSTRACT

This paper reports the first-ever study on nanoscale mineralogy in pyrite from the volcanogenic massive sulfide (VMS) deposits of the Iberian Pyrite Belt, southwestern Iberian Peninsula. It targeted colloform-textured grains formed at low temperature in the distal part of a polymetallic (Pb-Zn) massive sulfide lens hosted in felsic volcanoclastic rocks from the Masa Valverde deposit, and euhedral-textured grains (re)-deposited by higher temperature fluids in the Co-Au rich stockwork hosted in black shales of the Filón Norte orebody of the Tharsis deposit. The results acquired by a combination of techniques for mineral microanalysis and characterization (i.e., reflected light, FE-SEM, EPMA, LA-ICP-MS, HRTEM-STEM and TEM-EDS) show that trace amounts of metals (Au, Ag, As, Pb, Sb, Cu, Co) are incorporated as both lattice-bound and into nanoparticles (NPs). The mode of occurrence is strongly related with the evolutionary history of the mineralization. In the colloform pyrite collected from the massive sulfide lens, a rhythmic banding/oscillatory zonation with up to 3 wt% As, 5,000 ppm Pb, 1,070 ppm Sb and 750 ppm Cu is defined by the coexistence of several nano-sized layers (5 to 100 nm) and NPs (<100 nm) containing all these metals. The NPs include galena [PbS], tetrahedrite [$(Cu,Fe)_{12}Sb_4S_{13}$)] and arsenopyrite [FeAsS] that exhibit euhedral and less frequently anhedral (i.e., droplet-like) morphologies being both randomly and preferentially oriented with respect to As-rich pyrite bands they are usually associated with. These features suggest formation of the NPs via direct deposition from the hydrothermal fluid(s) or low-temperature melts entrained in them as well as exsolution of trace elements originally dissolved in the As-rich pyrite structure. Additionally, some of these NPs are connected to late fractures disrupting the chemical zoning in colloform pyrite documenting a third genetic type of NPs related to late infiltration of fluids post-dating pyrite formation. In contrast, euhedral pyrite from the stockwork form well-developed homogeneous grains with discrete porous areas relatively depleted in Fe (45.20 wt%), and As (8,800 ppm) but enriched in Co (5,900 ppm). At the nanoscale, Co-enriched domains show patchy zoning defined by irregular distribution of Co– and As-rich bands of 200–500 nm in thickness. These nanometer Co– and As-rich bands are often disrupted by micron-to-nano-sized polycrystalline Au-Ag-Hg particles that fill voids in porous areas. Contact morphology anatomy between Co-rich pyrite and inclusions suggests that the Au-Ag-Hg particles are negative crystals occupying spaces originated in pyrite by coupled dissolution-reprecipitation reaction. Likewise, HRTEM observations along such pyrite-inclusion contacts show the existence of polycrystalline matrices in both pyrite and Au-Ag-Hg inclusions, the former consisting of nano-sized domains of arsenian pyrite and/or arsenopyrite in As-free pyrite and the Au-Ag-Hg inclusions made up of multiple crystal domains including nano-crystallites of Au^0/Ag^0 or electrum. Recognition of crystalline nanodomains and NPs in these polycrystalline matrices raises the possibility that Au NPs or nanomelts already present in the hydrothermal fluid catalyzed the formation of these heterogeneous crystals.

* Corresponding author at: Instituto Andaluz de Ciencias de la Tierra, Consejo Superior de Investigaciones Científicas (CSIC)-Universidad de Granada, Avda. de las Palmeras 4, 18100 Armilla, Granada, Spain.
E-mail address: jmgonzj@ugr.es (J.M. González-Jiménez).
[1] ORCID: 0000-0001-7270-5227.

https://doi.org/10.1016/j.oregeorev.2022.104875
Received 17 January 2022; Received in revised form 24 March 2022; Accepted 6 April 2022
Available online 12 April 2022

1. Introduction

In the past two decades, a prodigious interest in nanoscience and nanotechnology has promoted a rapid development in the characterization of natural metal-based nanoparticles (hereafter NPs) and nanominerals (Hochella et al., 2008; Becker et al., 2010; Lee et al., 2016). In the physics and engineering literature, NPs categorize any particle having one or more dimensions in the range of 1 to 100 nm (10^{-9} to 10^{-7} m) whereas in mineralogy the terms apply to particles < 1 μm (Hochella et al., 2008). Mineral nanoparticles are particles of minerals that also exist in larger (micrometer-scale) sizes whilst nanominerals only exist within the nanoscale range (González-Jiménez and Reich, 2017). To date, nanoclusters (aggregates of tens to hundreds of atoms), NPs and areas with clustered NPs and nanominerals have been inferred to exist in some minerals from ore deposits (e.g., sulfides and oxides) by analyzing depth-profiling of element concentrations acquired by means of secondary ion-mass spectrometry (SIMS) and laser-ablation inductively coupled mass spectrometry (LA-ICP-MS) (e.g., Cook et al., 2009; Piña et al. 2012; Morishita et al., 2019; Torró et al., 2022), as well as imaged by other modern microanalytical techniques such as electron probe microanalysis (EPMA) and scanning electron microscopy (SEM) (e.g., González-Jiménez and Reich, 2017; Saunders et al., 2020; Ishida et al., 2021). However, many NPs and nanominerals contained in these minerals are smaller than 100 nm in size, making them "visible" only under more sensitive techniques such as the synchrotron X-ray fluorescence microscopy (XFM), the atom probe tomography (APT), high-angle annular dark-field scanning transmission electron (HAADF-STEM) or high-resolution (HRTEM-EDS) microscopy (Hough et al., 2011 and references therein).

Recent HAADF-STEM and HRTEM-EDS investigation of thin-foils obtained by using focused ion beam (FIB) from Ni-Fe sulfides (pyrrhotite, millerite, pyrite, pentlandite and chalcopyrite) of magmatic ores hosted in mafic–ultramafic rocks have shown a variety of PGE-dominated NPs, including alloys (Ir-Pt, Ru-Os, Pt-Au-Hg), sulfides (laurite [RuS_2]-erlichmanite [OsS_2] and unidentified compounds of Ru-Rh-Os, Ru-Rh-Pt-Ir, and Ru-Rh-Pt), arsenides (Rh-Rh-Pt-As), telluride [Pd-Te] and stannide [(Pt,Pd)Sn] (Wirth et al., 2013; Junge et al., 2015; González-Jiménez et al., 2018; Baurier et al., 2019; Jiménez-Franco et al., 2020; Xiong et al., 2021). The nanostructural relationship of these NPs with their host sulfide matrix along with the new synthesis of identical counterparts in high-temperature experiments confirm their indisputable early crystallization in the magmatic ore systems (see the review of González-Jiménez and Reich, 2017).

In contrast, the seeking of NPs in low and moderate-temperature mineral deposits of hydrothermal origin has been significantly biased towards the study of pyrite. Here, Au has been the most investigated element, being found as Au^0 NPs or combined with Ag (i.e., electrum) or other metals (e.g., Te, Pb) preferentially in As-rich domains of pyrite — i.e., arsenian pyrite defined as a pyrite containing from a few ppm to tens wt.% As (Abraitis et al., 2004; Qian et al., 2013; Reich and Becker, 2006; Deditius et al., 2014). Examples of Au-bearing NPs have been extensively documented in hydrothermal arsenian pyrite from porphyry Cu deposits (Reich et al., 2013), orogenic or sediment-hosted Carlin-type deposits (Palenik et al., 2004; Reich et al. 2005, Reich et al., 2006; Sung et al., 2009; Deditius et al., 2011) and epithermal Au-Ag (Pals et al., 2003; Deditius et al., 2011; Hough et al., 2011). However, the assemblage of NPs in hydrothermal arsenian pyrite is not limited to Au-bearing NPs but also include sulfides such as galena [PbS], cinnabar [HgS], chalcopyrite [$CuFeS_2$], arsenopyrite [AsFeS] and the tellurides nagyagite [$Pb(Pb,Sb)S_2(AuTe)$] and merenskyiite [$PdTe_2$] as well as a large suite of unidentified compounds comprising combinations of (semi)-metals (e.g., Deditius et al., 2008, 2011, 2014; González-Jiménez et al., 2021; Sung et al., 2009; Zhang et al., 2021). NPs within single grains of arsenian pyrite may be both crystalline and amorphous and share or not crystallographic continuity or orientation with the hosting sulfide matrix. Such nanoscale relationships led to different interpretations for the origin of the NPs in pyrite: (1) direct deposition of metal-bearing NPs from ions dissolved in hydrothermal fluids (Becker et al., 2010; Deditius et al., 2011, 2014; Zhang et al., 2021) or immiscible nano-sized liquids or particles (Saunders, 1990; Deditius et al., 2008; Saunders and Burke, 2017; Saunders et al., 2020; Hastie et al., 2021; Zhou et al., 2021; Petrella et al., 2021) eventually entrained in them; (2) solid-state exsolution of elements originally in solution in the arsenian pyrite lattice during post-crystallization events such as metamorphism (McMclenaghan et al., 2004; Reich et al., 2005) and/or deformation (Fougerouse et al., 2016, 2021); (3) metals liberated from the pyrite structure and shortly after precipitated as NPs during coupled dissolution-reprecipitation associated to *syn*-formational (Deditius et al., 2011) or post-formational (Xing et al., 2019) hydrothermalism.

An exception to the general rule to the intimate link existing between metal-based NPs and arsenian pyrite is the presence of Au-bearing NPs in As-free pyrite from the Dongping and Huangtuliang deposits in the Hebei Province, China (Cook et al., 2009; Ciobanu et al., 2011; 2012). In these intrusion-hosted Au deposits with orogenic overprint, composite NPs consisting of intergrowths of Au-Ag-bearing tellurides (petzite [$AuAg_3Te_2$], calaverite [$AuTe_2$], sylvanite-krennerite [$(Au,Ag)Te_2$], hessite [Ag_2Te]), altaite [PbTe] and Au^0 are intimately associated with microfractures and nanoscale porosity postdating primary Co-Ni zonation in As-free pyrite. These NPs having sizes of hundred(s) of nanometer were interpreted as the "frozen" solid expression of Te-rich, Au-Ag-Pb-bearing vapor discharged during the orogenic overprint long time after pyrite was formed (Ciobanu et al., 2012).

The observations above reveal that partitioning of many economic metals (e.g., Au, Ag, PGEs and base metals like As, Bi, Cd, Co, Cu, Mo, Ni, Pb, Se, Sb, Te, Zn; Watari et al., 2020) not only accounts as solid solution in iron-bearing sulfides from mineral deposits but also as metal-based nanominerals and NPs intimately associated to these sulfides. Studying the formation mechanisms of these NPs and nanominerals in ore deposits should therefore provide unique opportunities to explore the "missing link" between transport and deposition by fluids and melts necessary to unravel the genesis of economic mineral deposits. In addition, given their size, NPs and nanominerals have very high surface area to volume ratio, which also impart unique physicochemical properties that impact not only deposit genesis or in strategies for mineral exploration but also in metallurgical recovery and environmental mitigation of toxic elements in mining waste (e.g., Deditius et al., 2014 and references therein).

Despite of these advances on NPs inventory in sulfides from mineral deposits, to the best to our knowledge, there is no detailed information on the association of between NPs and pyrite from volcanogenic massive sulfide deposits (VMS). The presence of NPs consisting of Au, Ag, Te, Sb, Zn and/or Cd has indeed been suspected in pyrite, on the basis of elemental correlation data acquired by ion probe or LA-ICP-MS, from both fossil VMS from Canada (e.g., Bathurst Mining Camp, Bracemac-McLeod, and Caribou deposits; McMclenaghan et al., 2004; Genna and Gaboury, 2015; Wright et al., 2016), as well as inactive and active submarine hydrothermal vents (e.g., Trans-Atlantic Geotraverse (TAG), Turtle Pits and Comfortless Cove hydrothermal fields from the Mid-Atlantic Ridge Complex; Logatchev in the IRINA II Complex; Kairei and the Meso Zone from the Central Indian Ridge; Hine Hina and Jade from theValu Fa Ridge, and the Volcano 19 from Tonga–Kermadec arc; Keith et al., 2016). The only available work with an adequate nanoscale characterization of metal-based NPs in pyrite from this type of deposits is that of Deditius et al. (2011), who documented NPs from the hybrid VMS-epithermal deposit of Pueblo Viejo in the Dominican Republic. The suite of NPs identified by Deditius and co-workers include Ag^0, electrum and unidentified sulfides/sulfosalts (Cu-Fe-S, Pb-Sb-Bi-Ag-Te-S, and Pb-Te-Sb-Au-Ag-Bi-S). These NPs were interpreted to be originated through two complementary ways: (1) direct deposition from hydrothermal solutions and (2) exsolution from host pyrite during post-depositional changes such as heating.

This study focusses on a suite of spatially and paragenetically well-

constrained pyrite-bearing ores from VMS deposits of the Iberian Pyrite Belt (IPB) in southwestern Iberian Peninsula — the largest cluster of world-class VMS deposits exposed on the Earth's surface. This metallogenic province hosts more than 100 inactive or working mines, and includes the 22% of the world class VMS deposits (greater than32 Mt), classifying eight of them (Riotinto, Tharsis, La Zarza, Sotiel, Masa Valverde and Aznalcollar in Spain, and Neves Corvo and Aljustrel in Portugal) as giants (greater than100Mt) (Tornos, 2006 and references therein). Over the last five millenniums, it has intermittently been the major center of Europe's mining production of S, base (Cu, Zn, Pb) and precious (Au, Ag) metals (Pinedo-Vara, 1963; Nocete et al., 2005) with more than 1,600 Mt of massive sulfides and more than 2,500 Mt of stockwork mineralization (Leistel et al., 1998; Almodóvar et al., 2019). These metals have been mined in primary ores (i.e., massive sulfide lenses and stockwork) as well as their secondary products of supergene alteration (e.g., gossans; Yesares et al., 2017).

For this nanoscale study we have selected pyrite samples representative of the lower-temperature polymetallic and higher-temperature stockwork mineralization of the IPB. These include one of the two polymetallic Pb-Zn lenses hosted in felsic volcanoclastic rocks at the Masa Valverde deposit and a Co-Au stockwork hosted in black shales from the Filón Norte orebody of the Tharsis deposit, respectively). Data generated by scanning electron microscope (SEM) and high-resolution transmission electron microscopy (HRTEM) on individual pyrite grains are combined with electron probe microanalysis (EPMA) and LA-ICP-MS to better constrain the role of mineral nanoparticles in controlling concentration of base and precious metals in hydrothermal pyrite in this type of sulfide deposits. This improved understanding is used to provide insights on sources and mechanisms of enrichment of valuable metals in these hydrothermal systems, highlighting the possible implications for other deposits of this style worldwide and in particular the metallurgical beneficiation of unidentified resources.

2. Analytical methods

2.1. Electron microprobe analysis (EPMA)

The chemical compositions of pyrite were analyzed using a JEOL JXA-8200 Super Probe Electron Probe Micro-Analyzer at the University of Huelva, Spain. The measurements were performed on carbon-coated polished sections using an accelerating voltage of 20 kV, with 20nA beam current, 30 s counting time for the peaks and 10 s for the background measurements. The spots analyses were selected using backscattered electron (BSE) images. Concentrations of Ag, As, Au, Bi, Co, Cu, Cd, Fe, Hg, Ni, Pb, S, Se, Sb, Te, Zn in pyrite were determined by wavelength-dispersive spectroscopy (WDS). Routine data reduction, including full matrix (ZAF) corrections, were performed. The X-ray lines employed were Kα for S, Co, Fe, Ni, Cu and Zn; Mα for Hg, Au, Pb and Bi; Lα for Te, As, Ag, Se and Sb; and Lβ for Cd.

2.2. In situ LA-ICP-MS

Trace element concentrations on pyrite were analyzed by *in situ* LA-ICP-MS at the LabMaTer of the Université du Quebec à Chicoutimi, Canada. Samples were analyzed using an Excimer 193-nm Resolution M−50 laser ablation system equipped with a double volume cell S-155 and coupled with an Agilent 7900 mass spectrometer. The following isotopes were monitored, ^{34}S, ^{57}Fe, ^{59}Co, ^{60}Ni, ^{65}Cu, ^{75}As, ^{82}Se, ^{107}Ag, ^{121}Sb, ^{125}Te, ^{197}Au, ^{208}Pb, and ^{209}Bi. Laser spots of selected grains were made using a laser beam size ranging from 11 and 55 μm, a laser frequency of 15 Hz, and a fluence of 3 J/cm^2. An argon-helium gas mix was used as carrier gas. The gas blank was measured from 30 s before switching on the laser for 60 s. The ablated material was then analyzed using the mass spectrometer in time resolution mode using mass jumping and a dwell time of 10 ms/peak. Data reduction was carried out by the Iolite package of Igor Pro 8.0 software (Paton et al., 2011). Internal standardization was based on ^{57}Fe using the iron contents determined by electron microprobe. During data reduction, the entirety of the laser signal was integrated. We used the certified reference material MASS-1 for the calibration of the trace elements. It consists of a Zn-Cu-Fe-S pressed powder pellet provided by USGS and doped with 50–70 ppm of most chalcophile elements. The calibrations were monitored using GSE-1 g and UQAC-FeS1. GSE-1 g is a natural basaltic glass provided by the USGS doped with most elements at 300–500 ppm, and UQAC-FeS1 is an in-house Fe-S reference material doped with trace amounts of most chalcophile elements. Analyses of these materials agreed with the certified and working values.

2.3. Field emission scanning electron microscopy (FE-SEM) and focused ion beam (FIB)

Pyrite grains and their hosted mineral inclusions were preliminarily characterized and imaged using a Leo Gemini Field Emission Scanning Electron Microscope (FE-SEM) at the Centro de Instrumentación Científica of the Universidad de Granada, Spain. The instrument was equipped with an Energy Dispersive Spectra (EDS) detector. Accelerating voltage was 20 kV and beam current optimized for an adequate number of counts for each EDS analysis.

Four thin-foils samples (two from the inner and outer portion of the colloform pyrite from the massive sulfide lens of the Masa Valverde deposit and another two from the porous rim of euhedral pyrite from the stockwork of the Tharsis deposit) were prepared and extracted by using a Focused Ion Beam Scanning Electron Microscope (FIB-SEM) in the Laboratorio de Microscopías Avanzadas (LMA) at the Instituto de Nanociencia de Aragón (INA) – University of Zaragoza, Spain. The TEM thin foil preparation was performed using a Dual Beam FEI ThermoFisher Scientific, model Helios 650. The selected regions of interest containing inclusions were first covered by a thin strip (~300 nm) of C by focused electron beam induced deposition (FEBID) and subsequently with a second strip (~1 μm) of Pt. These strips act as protection during the milling, polishing, and extraction process of the thin foils. The bulk material was first removed on both sides of the lamella by a rough Ga^+ ion milling with a 30 kV current at 2.5nA and the subsequent polishing with a 30 kV current at 0.23nA. The final polishing step was performed on the sample's inclusions until the electron transparency was achieved. This was completed by subsequently milling the thin foil with a 5 kV current at 68 pA. The electron transparency was monitored by an Everhart-Thornley SE detector and using a 5 kV electron beam. After achieving the electron transparency, the thin foil was rapidly polished using a low energy 5 kV current at 10 pA to reduce the amorphization until a final thin foil thickness of ~ 90 nm was attained. Subsequently, the thin foil was undercut with a 30 kV at 2.5nA current, lifted out, and transferred from the sample to a TEM grid using an OmniProbe nanomanipulator with a tungsten tip. To weld the thin foil to the tungsten tip and the TEM grid, an ion-beam assisted Pt deposition was performed.

2.4. High-resolution transmission electron microscopy (HRTEM)

A combination of a Thermo Fisher Scientific TALOS F200X and a FEI Titan G2 transmission electron microscope (TEM) equipped with Field Emission gun XFEG was used to analyze the thin-foil at the Centro de Instrumentation Científica of the University of Granada, Spain. Both the TALOS and the FEI Titan G2 microscope are equipped with 4 energy dispersive analyses of X-rays (EDX) detectors (FEI microanalysis Super X) and a high-angle annular dark-field detector (HAADF). The FEI Titan G2 microscope also includes a spherical aberration corrector for the objective lens. Selected mineral areas of interest sampled within the thin-foils were imaged by the FEI Titan G2 microscope using a combination of high-angle annular dark-field (HAADF) to obtain Z high contrast images, and High-Resolution Transmission Electron (HRTEM) images to characterize the texture of the grains and to properly define the ordering of the mineral aggregates. All these images were treated

using the Digital Micrograph® software in its Version 1.71.38 while maps were processed with the VELOX® software package. The FEI Titan G2 was running at 300 kV working conditions while HRTEM images were acquired using Gatan CCD Camera. The Thermo Fisher Scientific TALOS F200X was employed for single-spot Analytical Electron Microscopy (AEM) analysis and to acquire compositional elemental mappings of the sample using 200 kV of accelerating voltage and image drift correction. Elemental maps images were also processed using the VELOX® software.

3. Geological and petrological background of pyrite samples

3.1. The Iberian pyrite belt

The Iberian Pyrite Belt (IPB) is a Paleozoic metallogenic province hosting the largest concentration of massive sulfide deposit worldwide. Here, the VMS deposits cluster within a fringe of 20–70 km that extend along more than 250 km through S Portugal and SW Spain (Fig. 1). On the basis of their geographical location and tonnage of the deposits, there are two main domains in the IPB (Fig. 1) known as (Sáez et al., 1999; Leistel et al., 1998; Almodóvar et al., 1998; Relvas et al 2001): (1) the northern belt dominated by larger number of smaller deposits (e.g., Lomero-Poyatos, Cueva de la Mora, Migollas and San Miguel) are mainly hosted mainly by felsic volcanic and volcaniclastic rocks, and (2) the southern belt dominated by less abundant but lager sized deposits are hosted by both black shales and felsic volcaniclastic rocks (e.g., Massa Valverde, Neves Corvo, Tharsis, Las Cruces, Aznalcóllar and Frailes).

Geologically the IPB belongs to the South Portuguese zone, which correspond to the southernmost zone of the Iberian Hercynian Massif. The accepted stratigraphy of the IPB includes, from bottom to top, the three following units: (1) the Phyllite–Quartzite Group (PQG) comprising shales quartz-sandstone, quartzwacke siltstones and minor conglomerate and limestones at the top of Givetian–Famennian age; (2) the Volcano–Sedimentary Complex (VSC) consisting of a lower subunit including mafic volcanic rocks, rhyolites, dacites and dark shales, and an upper one with dark, purple and other shales and volcanogenic/volcaniclastic rocks of late Famennian to mid-late Visean age; and (3) the post-volcanic Baixo Alentejo Flysh Group (in Portugal) or Culm Group (in Spain) of Visean–Bashkirian age. Most VMS deposits of the IPB are hosted in the felsic volcanic rocks and shales of the Volcano–Sedimentary Complex, which were collectively deformed during the Variscan orogeny. Overall, this deformational event resulted in a week metamorphism under prehnite-pumpellyite facies, although higher peak metamorphic conditions at greenschist facies (300–430 °C at 0.2–0.3 GPa; Marignac et al 2003; Castroviejo et al., 2011) has been reported restricted to shear zones and faults where strain and fluid migration was focused.

The samples analyzed in this study are pyrite-bearing ores from two VMS deposits (Massa Valverde and Tharsis) located in the Spanish side of the Iberian Pyrite Belt (IPB) (Fig. 1). These samples were collected well away from deformation zones as evidenced the preservation of primary textures or chemical zoning. Therefore, they are representative of the primal hydrothermal style of mineralization at low temperature (i.e., colloform-textured pyrite from Masa Valverde) and higher temperature (i.e., euhedral pyrite from Tharsis) preserved in VMS of the IPB (Marcoux et al., 1996; Leistel et al., 1998; Sáez et al., 1999; Ruiz et al., 2002; Almodóvar et al, 2019). Specifically, the colloform pyrite ores from Massa Valverde come from a drill core that intersected the peripheral part of the largest polymetallic (Pb-Zn) massive sulfide lens of this deposit (up to 70 m thick), which is hosted in the felsic volcanic rocks with interbedded tuffs and shales of the Volcano–Sedimentary Complex. The ore mineralogy of this polymetallic lens consists of pyrite, with subordinate amounts, in order of decrease abundance, of sphalerite, galena, chalcopyrite, tennantite-tetrahedrite and arsenopyrite, (Ruiz et al., 2002). The euhedral pyrite ores from Tharsis were collected from an open pit of the inner part of the stockwork of the Filón Norte orebody, which is one of the sixteen orebodies known in this deposit located in the Puebla de Guzmán anticline (Fig. 1). This Co-Au stockwork mineralization intersects a black shale horizon intercalated between the Phyllite–Quartzite Group and the Volcano- Sedimentary Complex. It consists of irregular veins composed by chlorite ± quartz ± cobaltite ± trace Bi–Pb–Cu–(Sb) sulphosalts, tellurides and native gold (Marcoux et al. 1996).

3.2. Petrological background of the samples

The colloform-textured pyrite from Masa Valverde consists of a core with multiple pitted spherical aggregates of pyrite framboids wrapped by packages of discrete pyrite layers (Fig. 2a). Single-spot analyses acquired by EPMA and line-profile LA-ICPMS data collected from the inner and outer portion areas where FIB lamellas were extracted (Fig. 2a) yield up to ~ 3 wt% As, along with detectable amounts of Pb (5,000 ppm), Sb (1,070 ppm) and Cu (750 ppm) and, at a lesser extent, Au (~7 ppm) and Ag (103 ppm) (Supplementary Appendix 1). A combination of EDS

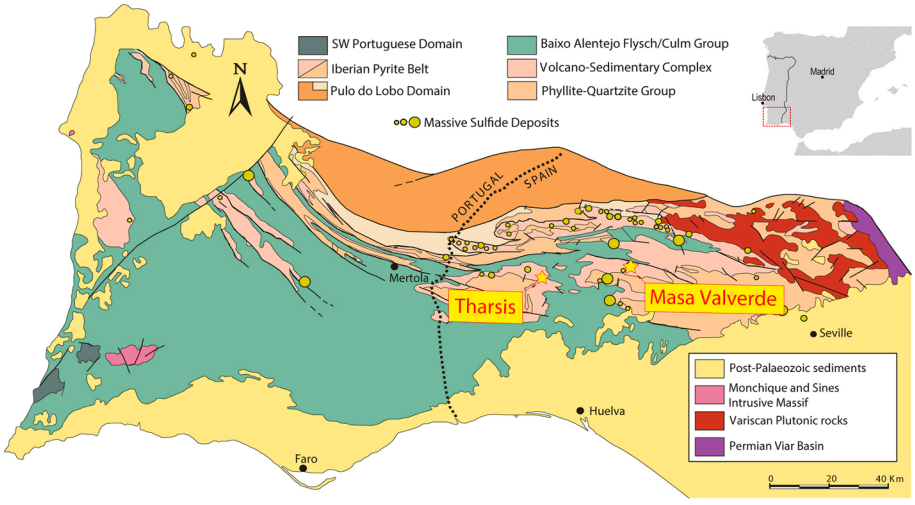

Fig. 1. Geographical location of the Iberian Pyrite Belt (IPB) in the the tectonic frame of south-western Europe (modified from Saéz, 2010) showing the location of the VMS deposits selected for this study.

spectra acquired by FESEM and X-ray EPMA mapping reveal the presence of abundant mineral micron- to nano-sized inclusions of As-Fe-S, Pb-S, and Cu-Fe-S-Sb in between or within these layers of pyrite, which are also detected in time-resolved spectra obtained by means of LA-ICP-MS (Fig. 3a-b). These mineral particles correspond to arsenopyrite [AsFeS] preferentially concentrated in the inner portions of the colloform arrangement, and galena [PbS] and tetrahedrite [$(Cu,Fe)_{12}Sb_4S_{13}$] in the outermost zone.

The euhedral-textured pyrite from the stockwork of the Tharsis deposit consists of euhedral pyrite with some perfectly well-developed external facets with discrete portions of the grains displaying high porosity with abundant solid inclusions (Fig. 2b). A combination of single-spot analysis collected by FESEM-EDS, X-ray EPMA mapping and LA-ICP-MS reveals that the porous area containing the Au-bearing particles analyzed here is depleted in Fe (45.20 wt%) and As (8,800 ppm), but is richer in Co (5,900 ppm) than the inclusion-free homogenous area (Fe = 46.78 wt%, As = 11,600 ppm and Co = 1,800 ppm) (Supplementary Appendix 1). The time-resolved spectra collected by LA-ICP-MS reveal abundant coupled ^{197}Au and ^{107}Ag spikes, confirming that Au-Ag-bearing particles imaged by FESEM-EDS and X-ray EPMA mapping (Fig. 2b) are also present at depth embedded within the porous area (Fig. 3c-d). Quantitative single-spot analysis obtained for the three largest Au-Ag-bearing particles using EPMA indicate that these mineral particles consist of 90.3–73.83 wt% Au, 7.08–19.76 wt% Ag and up to 3.22 wt% Hg (Supplementary Appendix 1).

4. Nanoscale study

4.1. Oscillatory zoning and (semi)-metal based nanoparticles of the colloform pyrite

The two thin foils performed from the inner and outer portions of the colloform pyrite from the Masa Valverde deposit successfully intersected the pyrite bands with variable amounts of As, Pb and Sb, as well as numerous solid inclusions consisting of these three elements (Fig. 4a-l).

The thin-foil #1 extracted from the inner portion of colloform arrangement directly enveloping clusters of pyrite framboids sampled an area with an oscillatory zoning defined by an alternance of ≤ 500 nm thick As-rich and As-poor pyrite bands (Fig. 4a-d and 5a). The HAADF-STEM image show intragranular micron- and nano-sized crack seal as well as pores and NPs < 100 nm in size within the As-rich bands (Fig. 4b and 5b). These images combined with the TEM-EDS area mapping also reveal that NPs containing Fe and/or As and/or Pb and/or Sb are preferentially located in the As-rich bands (Fig. 5a-b). The measured d-spacing from the HRTEM images indicates that NPs enriched in As display d-spacing of 2.81 Å matching the ideal reported in the literature for the plane (1 1 1) in arsenopyrite (Table 1). In contrast, those showing significant enrichment in Pb have a higher d-spacing of 3.42 Å matching that for the (1 1 1) plane of galena, and those with high Sb yield d-spacing of 3.65 Å that of the plane (2 2 0) of tetrahedrite [$(Cu,Fe)_{12}Sb_4S_{13}$] (Table 1). The HRTEM imaging and the SAED show that all metal-bearing NPs are crystalline but may show similar (arsenopyrite) or distinct (galena and tetrahedrite) orientation of their lattice fringes compared to their crystalline As-rich pyrite matrix (Fig. 5c-h).

The thin-foil #2 extracted from the outer portion of colloform pyrite also intersected oscillatory zoning (Fig. 4g-h) in this case consisting of an alternance of thinner bands (<5 nm to ~ 100 nm) with contrasting As-Pb contents (Fig. 4i-k, 6a-c and 7a-b). This zoning is often disrupted by microfractures hosting submicroscopic inclusions of galena (Fig. 4k and 6a-c). HAADF observation of the As-Pb-rich pyrite bands pictures the presence of several nanopores in these bands that were not identified in As-Pb-free pyrite bands (Fig. 6d) as well as a complex polycrystalline matrix with nano-sized domains (particles?) of arsenopyrite (Fig. 6e). Noteworthy, this thin-foil also intersected several NPs of tens nanometers size consisting of As and/or Pb and/or Sb attached at the contact between the As-rich and As-poor pyrite bands. The high-resolution images coupled with the qualitative TEM-EDS elemental map and point analyses confirm the existence of the same three types of crystalline nano-sized mineral nanoparticles identified in the thin-foil #1, namely arsenopyrite, galena and tetrahedrite (Fig. 7c-f). The structural observations (HRTEM images and corresponding selected area electron diffraction (SAED) patterns) of the three largest NPs sampled in this thin-foil reveal that they are hosted in polycrystalline matrices of As-rich and As-poor pyrite. A single crystal of tetrahedrite (Fig. 7d) and a twined nano-crystal of arsenopyrite (Fig. 7e) show common orientation to the heterogenous As-rich pyrite matrix (Fig. 7d-f and Table 1). In contrast, the smaller (~80 nm) grain of galena analyzed in this foil does not exhibit common crystallographic orientation with the As-rich pyrite matrix (Fig. 7c; Table 1).

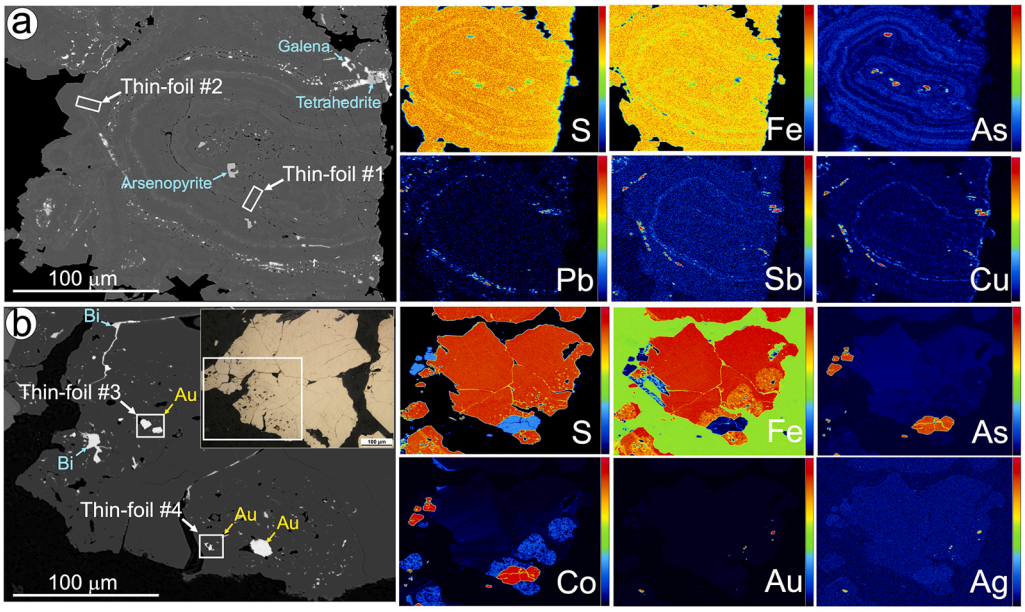

Fig. 2. Back-scattered electron images and corresponding quantitative X-ray EPMA maps of the pyrites selected for this study from the Masa Valverde **(a)** and Tharsis **(b)** deposits. Location of the four thin-foil sampled by means of FIB are inset in the figure.

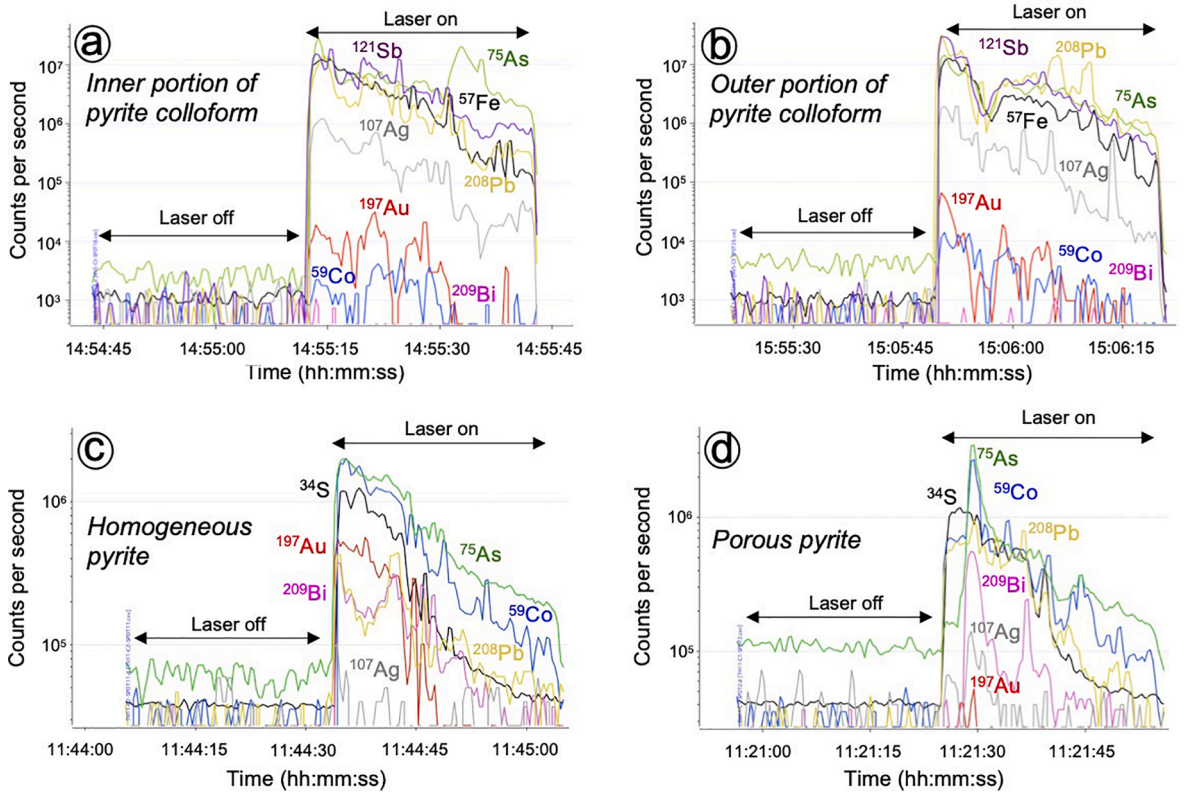

Fig. 3. Representative time-resolved LA- ICP-MS spectra collected during trace element analyses of pyrite showing the presence of several inclusions in the colloform (**a-b**) from the Masa Valverde deposit and recrystallized pyrite (**b-c**) from the Tharsis deposit.

4.2. Au-Ag-Hg alloys in porous rims of pyrite from the stockwork

Two micrometric Au-Ag-Hg particles —one euhedral and another anhedral on the surface of the polished thin section— located in the porous area of euhedral pyrite from the Tharsis deposit were successfully sectioned with the FIB (Fig. 8a-l).

The cross-section of the euhedral grain sampled by the thin-foil #3 revealed the characteristic feature of well-developed polygonal faces towards the contact with the host pyrite still at a depth of ~ 5 μm (Fig. 8a-f). The FIB-FESEM image shown in Fig. 8b reveal that the Au-Ag-Hg particle is an aggregate consisting of at least four euhedral domains weakly identified in TEM-EDS mappings (Fig. 8d-f). These TEM-EDS elemental maps of the area containing the inclusion and the hosting pyrite also reveal an irregular patchy zoning of As and Co in pyrite, which is an expression down to the nanoscale of the same zoning previously observed in X-ray EPMA mapping (Fig. 2b). This zoning is disrupted by the Au-Ag-Hg inclusion. The HRTEM observations and fast Fourier transform analyses (FFT) of the HRTEM images revealed that the four internal domains of the Au-Ag-Hg particle are themselves mosaic-like composite crystals made up of nanocrystallites with d-spacings of ~ 2.0 Å and 2.36 Å embedded in a matrix with more variable but wider lattice d-spacing (2.50 to 2.53 Å; Fig. 9a-b). Noteworthy, nanocrystallites are more abundant towards the contact with the hosting pyrite than in the inner portion of the Au-Ag-Hg inclusion. Further investigation of the grain boundary between the Au-Ag-Hg inclusion and pyrite reveals, in places, a crystalline As-rich pyrite matrix hosting particles with the aforementioned 2.0 Å d-spacing but with distinctively different orientation (Fig. 9c; Table 1). In other places, the SAED patterns allow us to identify two mismatched crystalline matrices: one corresponding to the As-rich pyrite host exhibiting d-spacings of 2.17 Å and 2.40 Å, and another one with d-spacing of 2.48 Å very likely corresponding to the Au-Ag-Hg inclusion (Fig. 9e-f; Table 1). Interestingly, those domains with the higher concentrations of Co and As located along and faraway from the contact with the Au-Ag-Hg inclusion display even higher d-spacings (3.72 to 3.89 Å; Fig. 9d and f) than those reported in the literature for pure pyrite (Table 1), thus confirming observations that entering of As (and very likely Co) promoted an expansion of the pyrite lattice.

The fourth thin-foil #4 that sampled the anhedral Au-Ag-Hg inclusion is also fully embedded in a crystalline sulfide matrix to a depth of ~ 3 μm (Fig. 8g-h). This inclusion, which exhibited an anhedral morphology on the surface of the polished, is characterized at depth by well-developed external outlines embayed against the host pyrite (Fig. 8g-h). The FIB-FESEM and HAADF imaging along with TEM-EDS mapping (Fig. 8i-l) reveal homogeneity within this grain. These TEM-EDS elemental maps of the area containing the inclusion and the hosting pyrite also reveal a sharp contrast between the alloy and pyrite, which is confirmed by HRTEM observations (Fig. 10a-b). However, transitional interface defined by a continuous stacking of layers with lattice rows yielding d-spacing of ~ 2.35 Å grading inwards to the Au-Ag-Hg consisting in a composite matrix with narrower (1.44 Å) and wider (2.47 Å) crystalline domains is observed (see SAED in Fig. 10c). On the other hand, in the sulfide matrix faraway from the contact with the Au-Ag-Hg inclusion, there are high-crystalline domains of pyrite and As-rich pyrite with locally higher d-spacings (2.55 or 3.56 Å) (Fig. 10d-f) intermediate between pyrite and arsenopyrite (Table 1).

5. Discussion

5.1. Origin of nanoscale chemical zoning and associated NPs in the colloform pyrite

Microscopic examination (i.e., reflected light, FE-SEM and X-ray EPMA mapping) reveal chemical variation of Fe, As, Pb, Sb and Cu across the whole colloform pyrite (Fig. 2a). The nanoscale study indicates that such variation is due to a rhythmic banding/oscillatory

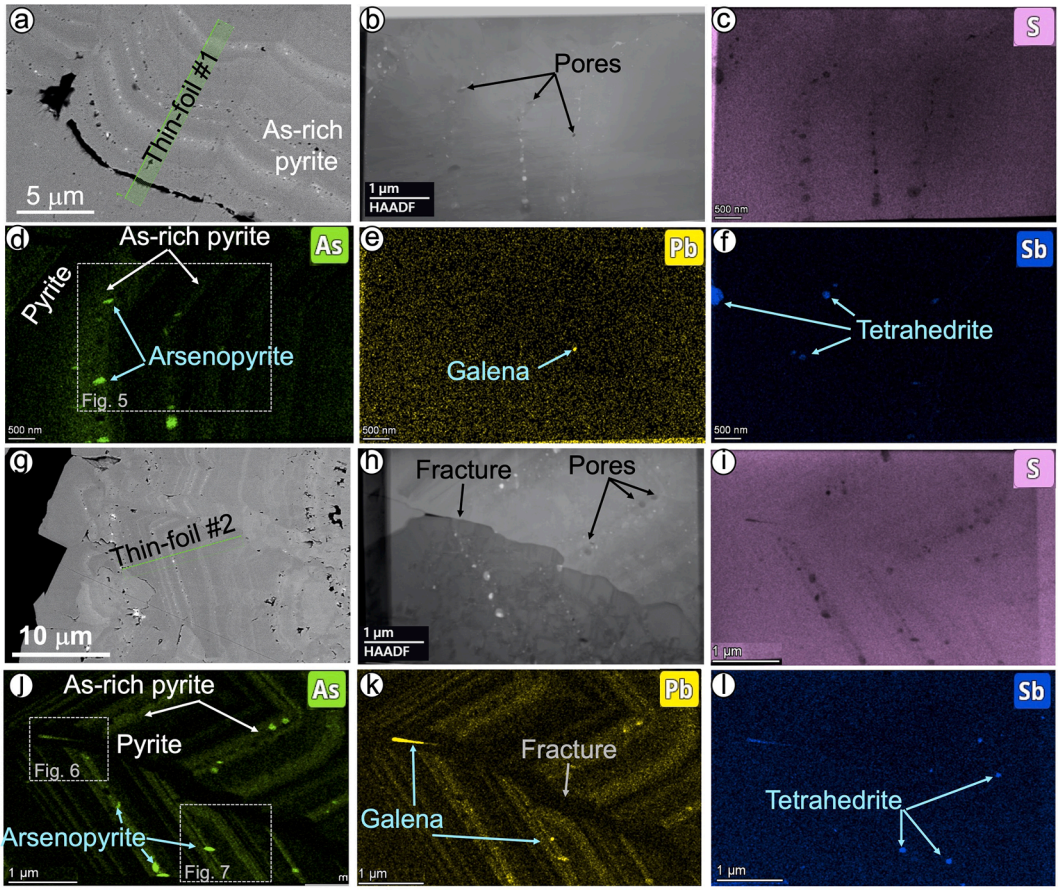

Fig. 4. A composition of back-scattered electron and negative HAADF images along with TEM-EDS elemental maps acquired for the inner (**a-f**) and outer (**g-l**) portions sampled by the thin-foil #1 and #2 respectively from studied pyrite colloform from the Massa Valverde deposit. Rectangles insets in (**d**), and (**j**) correspond to those areas investigated by HRTEM provided in the Figs. 5, 6 and 7 respectively.

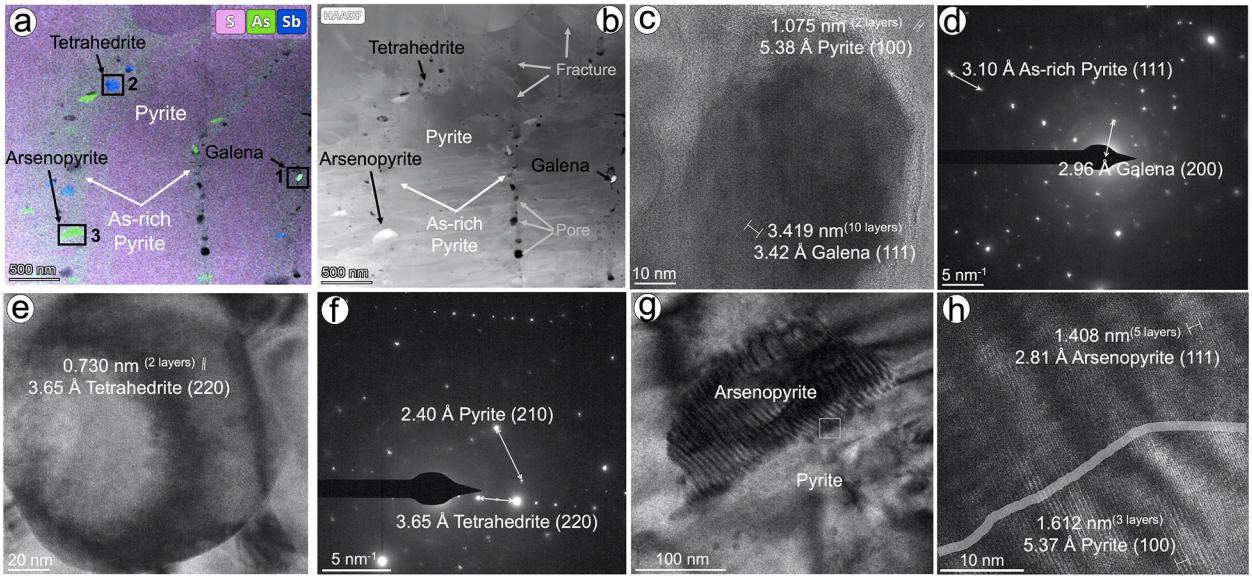

Fig. 5. Nanostructure of a selected area of the thin-foil #1 showing coexistence of nanoscale chemical zoning and metal-bearing NPs. TEM-EDS elemental and negative HAADF image of the selected area are shown in (**a**) and (**b**) respectively, whereas high magnification TEM images and corresponding SAED of NPs (galena, tetrahedrite and arsenopyrite) and host pyrite matrices are shown in (**c-h**). Black rectangles with numbers inset in (**a**) correspond to those NPs of galena (1), tetrahedrite (2) and arsenopyrite (3) shown in (**c-h**).

Table 1
Indexed SAED, FFT and HRTEM d-spacing values for As-rich pyrite matrices and NPs analyzed in this study compared with theoretical values from literature. Comparison data were acquired for pyrite by Bayliss (1977) and Rieder et al. (2007), arsenopyrite by Bindi et al. (2012), galena by Noda et al. (1987), tetrathedrite by Peterson and Miller (1986) and Foit and Hughes (2004), gold by Davey (1925) and Jette and Foote (1935), and silver by Wyckoff (1963) and Novgorodova et al, (1981).

(*hkl*)	(As-) Pyrite/arsenopyrite (measured d-spacing)	Pyrite (theoretical d-spacing)	Arsenopyrite (theoretical d-spacing)	Galena (measured d-spacing)	Galena (theoretical d-spacing)	Tetrahedrite (measured d-spacing)	Tetrahedrite (theoretical d-spacing)	Au-Ag-Hg (measured d-spacing)	Au^0 (theoretical d-spacing)	Ag^0 (theoretical d-spacing)
220								1.44	1.439/1.440	1.441/1.444
200								2.02	2.036/2.039	2.038/2.043
200								2.09	2.036/2.039	2.038/2.043
211/-212	2.17	2.211	2.199							
111								2.35	2.351/2.354	2.353/2.359
111								2.36	2.351/2.354	2.353/2.359
210/012	2.40	2.422	2.423							
−121	2.46		2.441							
								2.47	Not reported	Not reported
								2.48	Not reported	Not reported
								2.50	Not reported	Not reported
								2.53	Not reported	Not reported
−112	2.55		2.551							
002/200	2.66		2.678/2.676							
002/200	2.69	2.708								
	3.72		Not reported							
111	2.74		2.811							
111	2.81		2.811							
200				2.96	2.961					
111	3.10	3.126/3.127								
111	3.13	3.126/3.127								
111				3.42	3.420					
	3.56		Not reported							
220						3.65	3.649/3.652			
	3.76		Not reported							
	3.79		Not reported							
	3.81		Not reported							
011/110	3.89		3.898/3.896							
Cell (100)	5.37	5.38								
Cell (100)	5.38	5.38								

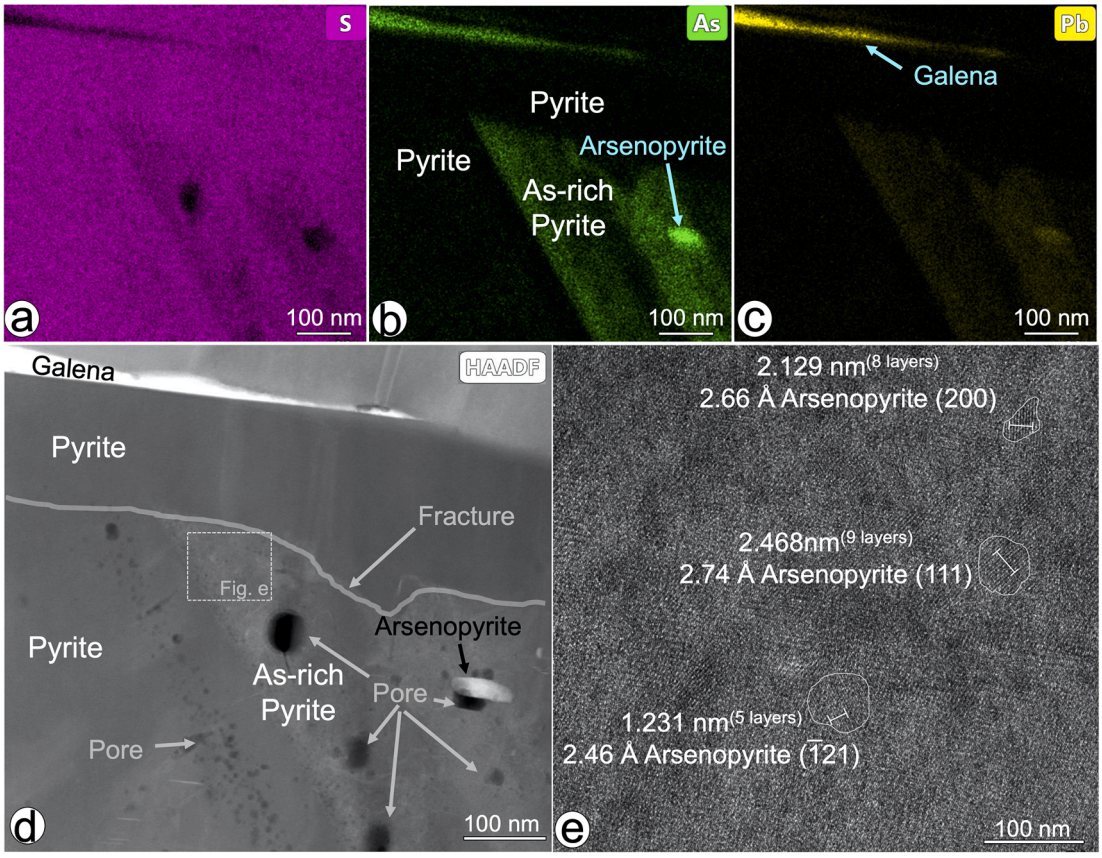

Fig. 6. Nanostructure of a selected are of the thin-foil #2 showing nanoscale chemical zoning disrupted by pyrite-filled fracture hosting a metal-bearing NPs of galena. TEM-EDS elemental and negative HAADF image of the selected area are shown in **(a-c)**, whereas **(d)** and **(e)** are the corresponding negative HAADF an HRTEM images.

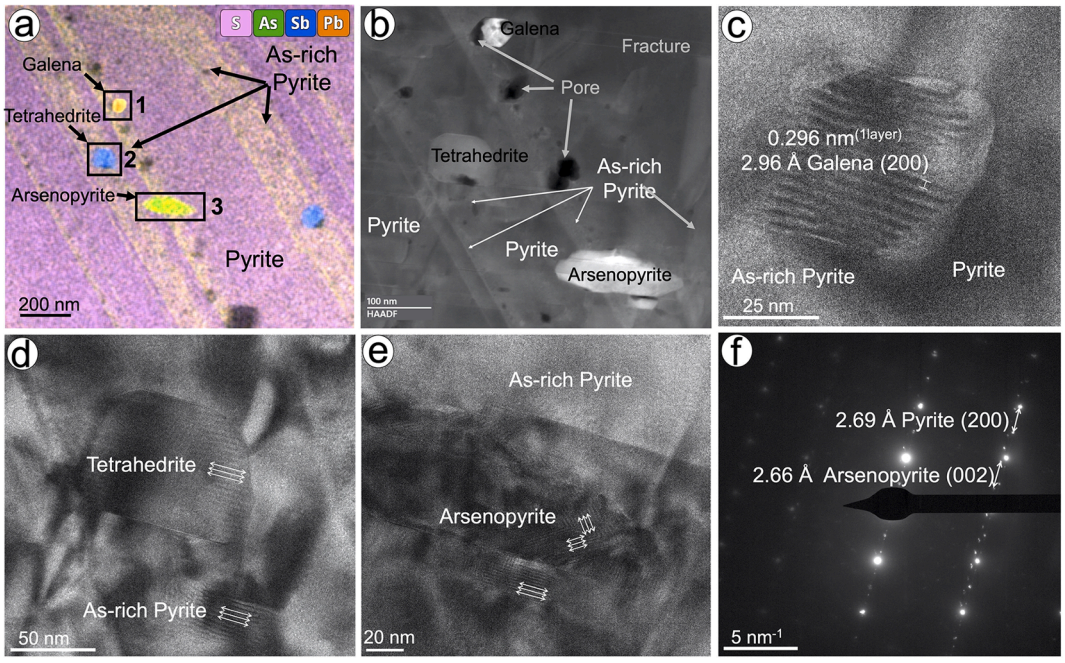

Fig. 7. Nanostructure of a selected are of the thin-foil #2 showing coexistence of nanoscale chemical zoning and metal-bearing NPs. TEM-EDS elemental and negative HAADF image of the selected area are shown in **(a)** and **(b)** respectively, whereas **(c-d)** are high magnification images of the NPs and their hosting pyrite matrices; **(f)** SAED pattern showing identical orientation of arsenopyrite NPs and host pyrite matrix. Black rectangles with numbers inset in **(a)** correspond to those NPs of galena (1), tetrahedrite (2) and arsenopyrite (3) shown in **(c-h)**.

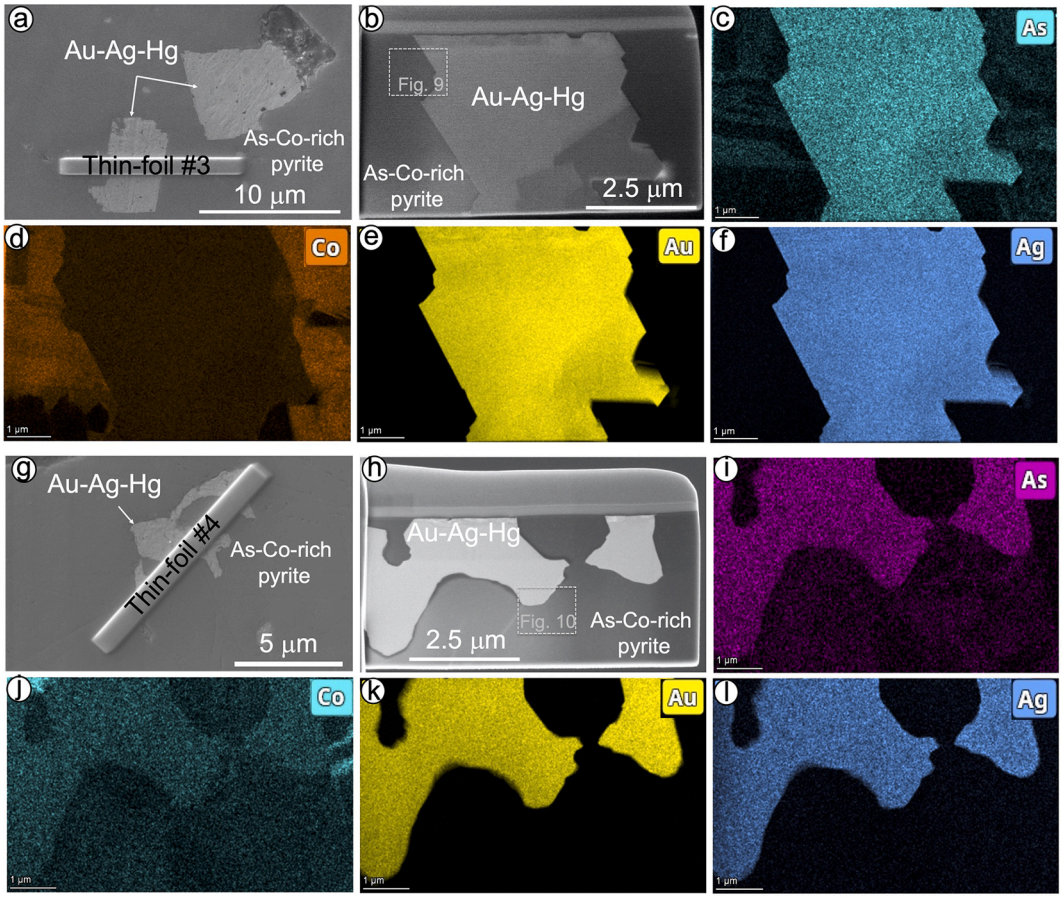

Fig. 8. A composition of back-scattered electron and negative HAADF images along with TEM-EDS elemental maps acquired for the euhedral (**a-f**) and anhedral (**g-l**) Au-Ag-Hg inclusions sampled by the thin-foil #3 and thin-foil #4 respectively from pyrite of the Tharsis deposit.

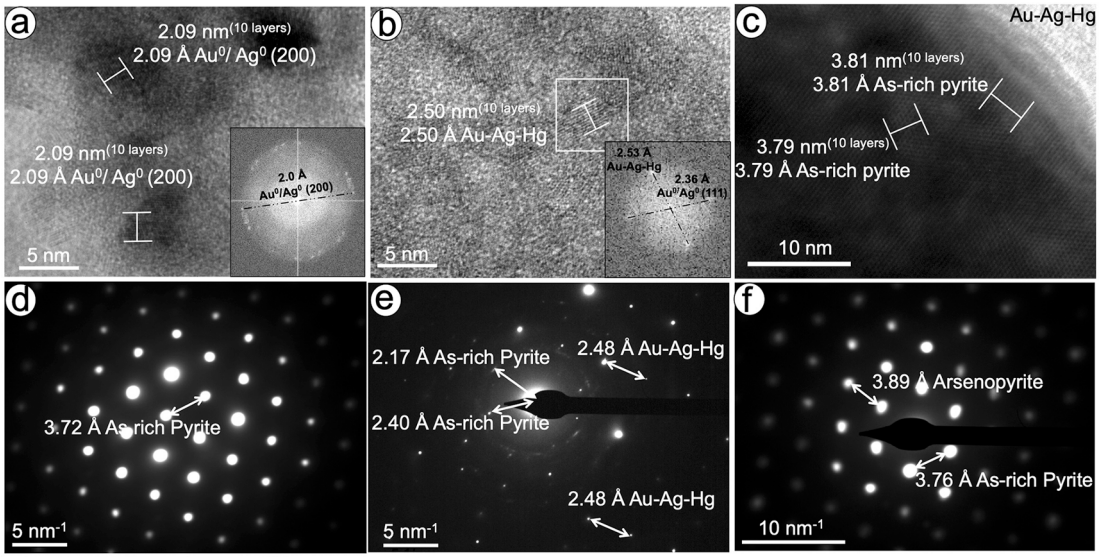

Fig. 9. Nanostructure of the contact between pyrite and hosted Au-Ag-Hg inclusion sampled by thin-foil #3 shown in Fig. 8b. (a-c) are HRTEM images with FFT inset, whereas (d-f) show SAED.

zonation of individual As-(Pb)-rich and Fe-S layers less than some tens of nanometers in thickness, with coexisting Sb-Cu-rich NPs (i.e., tetrahedrite) clustered in the As-(Pb)-rich bands (Figs. 4-7). These geochemical and mineralogical observations clearly track changes in the composition and physico-chemical conditions of hydrothermal fluid(s) involved in the formation of the colloform pyrite (e.g., Ishida et al., 2021).

The fact that As-Pb-rich bands are only present in the outer portion of the colloform pyrite documents the preferential entering of Pb at the latest stages of colloform crystal growth. It may be related with the infiltration of progressively hotter fluids enriched in base metals that

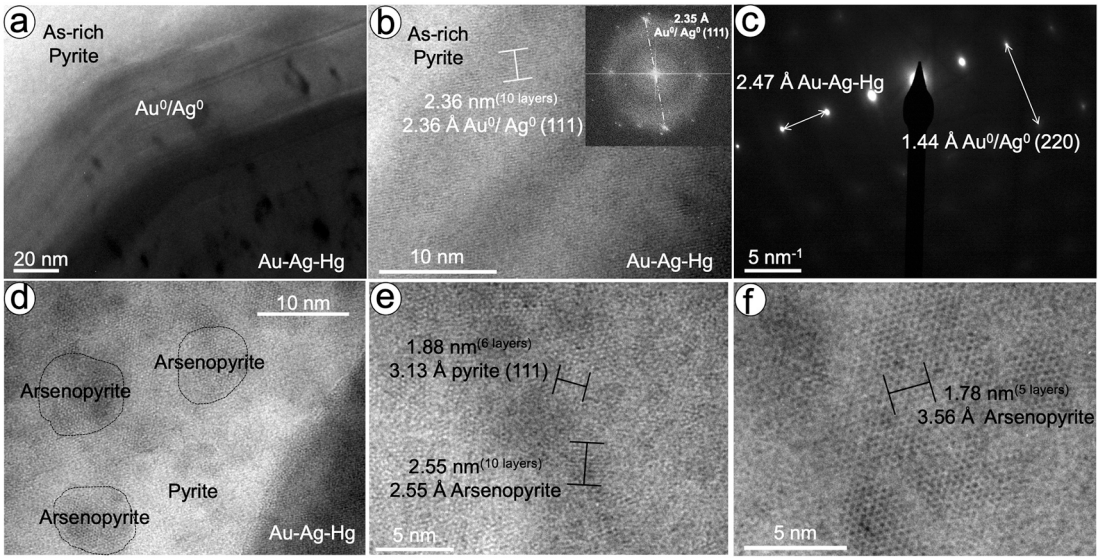

Fig. 10. Nanostructure of the contact between pyrite and hosted Au-Ag-Hg inclusion sampled by thin-foil #4 shown in Fig. 8h. HRTEM images with FFT inset and SAED for the Au-Ag-Hg inclusion are shown in (**a-c**), whereas HRTEM images the nanostructure of the pyrite host in the proximities of the contact with such inclusion are shown in (**d-f**).

promoted maturation of the pyrite texture; from < 100 °C during the formation of the pyrite framboids (Almodóvar et al., 1998) to up to 200–300 °C in the outer portion of the colloform (Almodóvar et al., 1998; Sáez et al., 1999). The coupled behavior of As and Pb in the outer portion of the colloform pyrite has its expression at the nanoscale by the presence of nano-sized domains (nanoparticles?) with d-spacing fitting arsenian pyrite (Fig. 6e and Table 1). In addition, whilst there is no corrosion rinds and truncated zoning within the inner portion of the colloform texture sampled by the thin-foil #1 (Fig. 4a-d and 5a-b), they could be observed in some areas of the outer portion of the colloform pyrite sampled by the thin-foil #2 (Fig. 4g-l and 6a-d). Overall, these nanoscale observations document an almost continuous growth at the initial stages of formation of the colloform structure —at expenses of pre-existing nuclei of clusters of pyrite framboids— with certain equilibrium between advancing crystallization surfaces of the pyrite crystals and local fluids. In these initial stages of colloform growth, selective partitioning of trace elements and crystal growth rates should exceed the lattice diffusion rates, contrarily to the culminating stages which were characterized by growth of the colloform with events of dissolution and re-precipitation promoted by an intermittent supply of metals near the surface of the growing pyrite.

On the other hand, the coexistence of NPs and nanoscale chemical zoning in pyrite clearly suggests a dual mechanism of incorporation of metals during the formation and evolution of the colloform pyrite, as already documented in hydrothermal pyrite from many different styles of hydrothermal mineralizations elsewhere (e.g., Deditius et al., 2011). The observation that randomly oriented galena NPs are preferentially attached the edges of the As-(Pb)-rich pyrite bands of the inner and outer portion of the colloform (Fig. 5a-c and 7a-c) suggests co-precipitation of these metal-bearing NPs and As-rich pyrite. Moreover, similar relationships and droplet-like morphology displayed by tetrahedrite NPs and host sulfide matrix in the inner portion of the colloform structure (Fig. 5e-f) is also compatible with formation of metal-bearing NPs via direct deposition rather than exsolution (Jian et al., 2022). The fact that these NPs are attached to arsenian pyrite surfaces highlights the key role played by arsenian pyrite in promoting the stabilization of metal-bearing NPs (Becker et al., 2010; Deditius et al., 2011, 2014). Previous works have shown that when As (i.e., As^{-1}, As^{0}, As^{+3}) substitutes S or Fe in pyrite, it induces an expansion of the structure due to the larger effective ion radius of As relative to that of S and Fe (Simon et al., 1999; Blanchard et al., 2007; Deditius et al., 2008; Kesler et al., 2010; Merkulova et al., 2019; Zhang et al., 2021). Such expansion of the crystal lattice promotes the development of crystal defects (e.g., Fleet et al., 1989; Simon et al., 1999; Palenik et al., 2004) resulting in electrically imbalanced growing surfaces. These mineral surfaces are ideal for reactive destabilization (e.g., chemisorption) of metal–ligand complexes carried by the hydrothermal fluid, thus leading the observed non-oriented growth of NPs (Fleet and Mumin, 1997; Li et al., 2012; De Yoreo et al., 2015; Jian et al., 2022; Ishida et al., 2021). TEM-EDS mapping of our colloform-textured pyrite reveals antithetic As-S correlation (Fig. 4c-d and i-j) consistently with As by S substitution, whereas HRTEM and SAED data confirm such expansion of the pyrite lattice (Table 1).

Moreover, the presence of tetrahedrite inclusions with drop-like morphology (e.g., Fig. 5e) raises the possibility of a mechanical entrapment of an immiscible volatile-rich fluid/melt (Ciobanu et al., 2012). The contribution of a volatile-rich fluid/melt during NPs formation is also suggested by the presence of abundant nanopores in these As-rich pyrite bands (Fig. 5b), which would nucleate or stabilize on the more reactive As-rich pyrite surfaces too. The formation of a metallic melt could account through adsorption–reduction mechanisms on the pyrite surfaces via direct scavenging of metals from aqueous fluids (e.g., Tooth et al. 2008, 2011) without a requirement for the ore fluid to be saturated with the constituent metals (Jian et al. 2021). These melts could therefore efficiently partition low melting point chalcophile elements such as As, Sb or Cu that now form NPs and other micron-sized inclusions in colloform pyrite. Polymetallic melts containing the aforementioned elements may survive down to very low (<300 °C) temperatures (e.g., Frost et al., 2002). For instance, experiments of partial melting conducted for the Fe–Cu–Pb–Sb–As–S compositional system indicate that As–S compounds melt at < 115 °C whereas As–(Fe)–S melts appear at 281 °C in the ternary As–Fe–S and Cu–As–S systems (Hall and Yund, 1964; Maske and Skinner, 1971; Chang and Bever, 1973). A first melt containing Pb, Sb and S forms in the metal-rich portion of the Pb–Sb–S system at 240 °C (Craig et al., 1973) and at slightly higher temperatures of 305 °C in the system Pb–As–S. In addition, melting temperatures of metal-bearing NPs is size-dependent and decrease dramatically at the nanoscale compared with bulk counterparts (e.g., Buffat and Borrel, 1976; Castro et al., 1990; Burda et al., 2005; Becker et al., 2010). However, the limited available data on the stability of polymetallic (Fe–Cu–Pb–Sb–As–S) melts at the nanoscale range does not permit to dismiss or confirm the possibility that some of the NPs

identified in the studied colloform pyrite precipitated directly from low-temperature melts. At least, some of the temperatures are geologically reasonable because they overlap the aforementioned temperatures of formation of colloform pyrite estimated by fluid inclusion studies for polymetallic massive sulfide lenses in VMS deposits from the IPB (~250 °C; Almodóvar et al., 1998). In the proposed scenario, the precipitation of metal-based NPs vs solid solution in pyrite should reflect the fact that the hydrothermal fluid became somehow locally supersaturated in metals far beyond the solubility limit of pyrite (e.g., Deditius et al., 2014).

In contrast, other tetrahedrite and arsenopyrite NPs show internal crystallographic features alienated with host pyrite (Fig. 5g-h and 7d-f). Although oriented attachment on growing As-rich pyrite surfaces could effectively account, an origin of these NPs related to the exsolution of certain elements originally retained in solid solution in the pyrite lattice cannot be completely ruled out (e.g., Zhang et al., 2021). Indeed, the nano-sized domains (nanoparticles?) of arsenian pyrite imaged within the As-Pb-rich bands (Fig. 6e) may provide evidence for the heterogeneous dissolution of metals in these pyrite bands.

Finally, larger galena and arsenopyrite NPs identified in the outer portion of the colloform pyrite are associated with fractures disrupting the As- and Pb-rich growth bands (i.e., NPs enclosed in the rectangles inset in Fig. 4j corresponding to the areas shown in Figs. 6 and 7). That these NPs are connected with the healed crack-seal of pyrite support their full crystallization in crack-seal postdating pyrite solidification, which may be linked to refining processes related with both the on-going late hydrothermal activity and/or the Hercynian deformation metamorphism (Almodóvar et al., 2019). In this scenario, that NPs are both unoriented (galena) and oriented (arsenopyrite) relative to the host pyrite highlight the complexity of fluid–solid interaction at the nanometer scale during these latter processes, which are still poorly understood (e.g., Lee et al., 2016). It is worth to note that similar nanoscale relationships with Au-bearing NPs disrupting Co-Ni zonation in As-free pyrite have been documented in the Dongping and Huangtuliang deposits in the Hebei Province, China (Cook et al., 2009; Ciobanu et al., 2011, 2012). In this latter case, NPs were interpreted as the "frozen" solid expression of metal-bearing vapor discharged during the orogenic overprint long time after pyrite was formed (Ciobanu et al., 2012).

5.2. *Fluid-mediated coupled dissolution-reprecipitation of pyrite promotes formation of polycrystalline Au-Ag-Hg*

Pyrite from the Tharsis deposit display porous zones enriched in Co containing abundant Au-bearing NPs (Fig. 2b). Such chemical variation identified at the micron-scale by means of FE-SEM, X-ray EPMA maps and single-spot LA-ICP-MS has also its expression down to the nanoscale by a patchy zoning defined by irregular distribution of Co– and As-rich bands of 200–500 nm in thickness (e.g., Fig. 2b and 8c-d). HAADF-STEM and TEM-EDS investigation of these porous zones in pyrite shows that Au-Ag-Hg particles disrupt the continuity of these irregular Co– and As-rich bands (Fig. 8c-d), evidencing their later origin. Consistently, SAED data show mismatch in the orientation of the lattice fringes of the Au particle and hosting pyrite (Fig. 9e). In this regard, the anatomy of the contact between Au-Ag-Hg inclusions and pyrite characterized by mutual embayment suggests that Au-Ag-Hg are negative crystals occupying spaces indeed originated in pyrite. This later observation along with fact that in places there is a sharp boundary between the Au particle and host pyrite defined by a stacking of Au^0/Ag^0 growth bands (Fig. 10a) suggest a mechanism of coupled dissolution-reprecipitation reaction (CDRR; Putnis, 2002; Xia et al., 2009; Sung et al., 2009). Here, this mechanism proceeded via the complete dissolution of the pre-existing As-poor pyrite while promoting micron-scale porosity, coupled at the nanometer scale with precipitation of polycrystalline As-Co-rich pyrite and Au-Ag-Hg particles.

HRTEM investigation suggests that the polycrystalline As-Co-rich pyrite matrix is due to a heterogenous mix of two different matrices consisting of As-free pyrite and arsenopyrite(see whole set of measurements in Fig. 9c-f, Fig. 10d-f and Table 1). The d-spacings 2.17 Å and 2.40 Å identified by means of SAED in the thin-foil 3 (Fig. 9e) are lower than the 2.21 Å and 2.42 Å d-spacings corresponding to (211) and (210) of pure pyrite, but slightly closer to the 2.19 Å and 2.42 Å d-spacings corresponding to (−212) and (012) of arsenopyrite (Table 1). In contrast, the constant d-spacing 2.55 Å measured in the sulfide matrix faraway from the contact with the Au-Ag-Hg inclusion in the thin-foil 4 (Fig. 10e-f) is not present in pyrite but in various interplanar hkl of arsenopyrite (Table 1). Moreover, the set of d-spacings ranging from 3.56 Å to 3.81 Å (Fig. 9c-d and 10f) are not identified in pure arsenopyrite and may be interpreted as intermediate between both structures. Finally, the d-spacing 3.89 Å overlap (Fig. 9f) within error d-spacing varying from 3.87 to 3.89 Å recognized in several planes of arsenopyrite (Table 1). These variations in the chemistry and d-spacing may reflect the distortion of the original pyrite matrix as a result of CDRR processes.

Similarly, the two particles of Au-Ag-Hg sampled in thin-foils #3 and 4 are polycrystalline. As seen in Figures 9a-c and 10a-c they are heterogenous aggregates of nano-sized crystallites with d-spacings from 1.44 to 2.3 Å embedded in a crystalline matrix with wider inter-atomic spaces (2.50 to 2.3 Å). The interplanar spacings 2.0 Å and 2.36 Å identified in the two particles analyzed here (Figs. 9a-b and d) fit well with the interplanar spacing (200) and (111) of the fcc structures of both Au^0 and Ag^0 (Table 1). Seemingly, the measured d-spacing of 1.44 Å identified in the thin-foil #4 (Fig. 10c) also matches well with the d-spacing 1.44 Å of (220) of both Au^0 and Ag^0 (Table 1). However, due to very similar lattice constant values of Au^0 (4.08 Å) and Ag^0 (4.09 Å), it is not possible to decipher whether these particles are single domains of Au^0, Ag^0 or a combination of both. The TEM-EDS maps acquired for these nano-scale domains reveal a homogenous distribution of Au and Ag at the relevant scale, leading to the suggestion that these particles could correspond to bimetallic nanocrystals of electrum instead of simple mixture of monometallic particles of Au and Ag. It is worth to note that Sánchez-Ramírez et al. (2008) synthesized nanocrystals of electrum with d-spacings identical to those measured here, i.e., 2.35 Å corresponding to (111) of electrum with Au/Ag = 1/1 and 2.04 Å for metallic ion solution with Au/Ag = 1/3. The results of these authors highlight that individual nano-domains with varying Au/Ag ratios may also exhibit significant differences in the interplanar spacings, with the entering of Ag promoting more closet packaging of the structure and therefore reduction of interplanar d-spacing. Thus, the d-spacings varying from 1.44 to 2.3 Å observed in our nanocrystallites may reflect alloying of Au and Ag at varying abundances. In contrast, wider inter-atomic spaces of 2.50 to 2.53 Å forming the matrix hosting these nanocrystallites may be assigned to the entering of Hg in the structure. Structural studies of Au-Au-Hg alloys indicate that increasing contents of Hg effectively result in a distortion (i.e., expansion) of the Au^0, Ag^0 or electrum structures owing the higher average metallic radius of Hg (1.55 Å) relative to Ag (1.45 Å) and Au (1.44 Å) (Massalki, 1957; Wells, 1984; Bindi et al., 2018). Single EPMA data indicate that the inclusions may contain up to 3 wt% Hg, which is enough to promote the observed variations of lattice parameters.

Recognition of the Au-Ag-Hg inclusions made up of multiple crystal domains including of nano-crystallites of Au^0/Ag^0 or electrum raises the possibility that NPs catalyzed the formation of these heterogeneous crystals. In the classical crystallization theory, crystal growth is described as the addition of atoms or ions (i.e., building blocks) to the crystal lattice (Lee et al., 2016 and references therein). Furthermore, the formation of heterogenous (polycrystalline) crystals is related to the growth of randomly oriented crystalline domains because of defects, which may account by the addition of impurities when building blocks are supplied at solid–fluid interfaces. In reality, however, this classical model reflects only a part of the picture because heterogeneous crystal growth may be also achieved by assembly and merging of NPs (Wang et al., 2014). In our study case, the higher abundance of nanocrystallites of Au^0/Ag^0 or electrum in the proximities to the contact with host pyrite

(e.g., Fig. 9a-b) suggests that NPs played a key role in the formation of the polycrystalline structure of the Au-Ag-Hg inclusions. These NPs occurred as a short-lived intermediary between metal ions in true solution and the larger polycrystalline Au-Ag-Hg mineral during the earlier stages of CDRR (Hochella et al., 2008; Lee et al., 2016), while their preservation should have been favored at the reaction front of the dissolving pyrite representing a disequilibrium frontier (Cölfen and Antonieti, 2005; Fang et al., 2011; Zhou and O'Brien, 2012). In fact, recent studies have already suggested that micron-sized crystals of Au with variable amounts of Ag and other trace elements may form via the assembly of smaller "precursor" Au NPs eventually carried by fluids or originated at the solution-solid interfaces (e.g., Saunders and Burke, 2017; McLeish et al., 2021; Hastie et al., 2021; Petrella et al., 2021). The small size (≤10 nm) of many of the NPs identified here would suggest colloidal stabilization soon after the NPs nucleation. Fluid inclusion studies (Almodóvar et al., 1998; Nehlig et al.,1998; Marignac et al., 2003) indicate that metal (re)-deposition in stockworks of the IPB was dominated by high-temperature (~350 °C), acid, oxidant high-saline fluids with low sulfur activity. Under these conditions, chloride complexes ($AuCl_2^-$) were the dominant carriers of Au, Ag and Hg in aqueous solid solution (Huston and Large, 1989; Leistel et al.,1998; Seward et al., 2014). It is very likely that once these fluids interacted with pyrite it promoted the "*in situ*" destabilization of these complexes and concomitant nucleation of the precursor Au-bearing NPs (e.g., McLeish et al., 2021). This milieu locally saturated with respect to gold/electrum shifted later to a later growth by coalescence or Ostwald ripening in order to produce the micron-scale ingrowth of the Au-Ag-Hg inclusions (Polte, 2015; McLeish et al., 2021). Our observations do not permit to dismiss or confirm the possibility that precursor Au NPs could be formed *in situ* at the pyrite reaction front from certain amount of Au liberated from the host pyrite during the CDRR processes instead to be supplied by the hydrothermal fluid alone (e.g., Hastie et al., 2021). However, single-spot data indicate relatively higher amounts of Au in in the porous zones than in homogeneous inclusion-free areas of this pyrite type. This observation suggests that although few amounts of Au could be certainly released from the pyrite host, most of it was probably supplied by the infiltrating fluid that produced alteration of pre-existing pyrite. On this line, we should stress that a number of experimental (Frens, 1973; Weitz and Huang, 1984; Liu et al., 2019) and empirical (Saunders, 1990; Herrington and Wilkinson, 1993; Harrichhausen, 2016; Saunders and Burke, 2017; Burke et al, 2017; Hannington and Garbe-Schönberg, 2019; Prokofiev et al., 2020; McLeish et al., 2021) works have provided substantive evidence that hydrothermal fluids relevant for the formation of a range of mineral deposits (epithermal, carlin, porphyry) might carry Au as suspended NPs. The recent documentation of Au NPs in sub-aerial geothermal systems (Hannington et al., 2016; Kanellopoulos et al., 2017) and submarine hydrothermal vents (Gartman et al., 2018) suggests that Au NPs may be also important contributors to VMS deposits. This mechanism of Au transport known as "colloidal" can concentrate up to ~ 5,000 times more Au in solution than as dissolved species (Liu et al., 2019), with NPs able to form at any time of the evolution of the hydrothermal ore system (Petrella et al., 2021). However, we do not have compelling evidence supporting that in the hydrothermal ore system of Tharsis, Au was physically transported in the hydrothermal fluid over large distances. This is clearly a fertile field for further investigation.

On the other hand, the voids of porous pyrite from Tharsis containing the Au-Ag-Hg particles also host a plethora of minerals of the Bi-Te-Cu-Se-Sb-S system (Marcoux et al., 1996; Leistel et al., 1998), including Bi^0 (Fig. 2b). This highlights that precursor NPs might also form via solidification of nano-sized Au- and Ag-rich polymetallic melts enriched in low melting point chalcophile elements (LMCE) such as Bi, Te or Sb. Some recent studies support Au concentration by LMCE-rich melts in hydrothermal fluids, including those typically involved in the formation of VMS deposits (Tooth et al., 2011; Zhou et al., 2017). In addition, there is now abundant evidence for a genetic role for polymetallic melts as an alternative mechanism for Au deposition in a range of hydrothermal deposits (McCoy, 2000; Cook and Ciobanu, 2004; Cepedal et al., 2006; Guimarães et al., 2019; McFall et al., 2018; González-Jiménez et al., 2021; Jian et al., 2022) as well as in modern VMS systems (e.g., Southern Gorda Ridge; Toermanen and Koski, 2005). Experimental (Douglas, 2000; Tooth et al., 2008) and empirical (Farrow and Watkinson 1992; Ciobanu et al., 2005, 2010; Jian et al., 2022) results in the Au-Ag-Te-Bi-Na-Cl-S-H-O system show that Au-Te-Bi-rich melts may separate from hydrothermal fluid at anytime during their cooling path at temperatures as low as 300 °C down to 135 °C. For example, native Bi melts at 271 °C whereas Bi-rich polymetallic assemblages of Au-Bi have an eutectic at 241 °C. Likewise, polymetallic melts consisting mainly of Au, Ag, and Te with additional Fe, S, Cu and Pb have been documented in some hydrothermal lode gold from Xiaoqinling in Central China at temperatures as low as 135 °C (Jian et al. 2021). All these temperatures are much lower than temperature estimated for the precipitation of hydrothermal pyrite during the formation of the IPB stockwork ore systems (~350 °C; Almodóvar et al., 1998) and their later overprint by metamorphic-related hydrothermal fluids (up to 380 °C maximum; Marignac et al., 2003). On this line the infilling nature of the Au-Ag-Hg particles in pores within pyrite evidences the existence of Au-bearing polymetallic nanomelts in the studied samples, although the primary hydrothermal vs. metamorphic-related hydrothermal origin of these metals is uncertain. It is noteworthy that nano to-micron-sized Au-rich polymetallic droplets trapped as primary melt inclusions have been recently identified in hydrothermal pyrite from the Kenty Au deposit in Canada (Hastie et al., 2021) and the Xiaoqinling Au district in China (Jian et al., 2022), concluding that a combined transport of Au by nano-sized melts and NPs is possible in hydrothermal ore systems at the nanoscale realm. Although demonstrated for Fe-As-S (e.g., Deditius et al., 2008), the role of nanomelts in controlling Au partitioning in hydrothermal melts have not been explored yet in experiments. If nanomelts were entrained in the hydrothermal fluids involved in the formation and evolution of the Tharsis deposit it could overcome the high Au enrichment in the studied samples, providing an alternative/complementary mechanism to those discussed above.

6. Conclusions

This study provides the first ever nanoscale characterization, using a combination of FIB-HRTEM, of hydrothermal pyrite from volcanogenic massive sulfide deposits of the IPB. The analysis of pyrites from the Tharsis stockwork and Masa Valverde polymetallic (Pb-Zn) massive sulfide lens of this metallogenic province reveals a complex nanoscale structure. Chemical zoning in terms of Fe, As, Pb, Sb and Cu in colloform pyrite from the polymetallic mineralization formed at < 300 °C is related to individual (<10 nm) As-(Pb)-rich and Fe-S layers as well as abundant NPs of arsenopyrite, galena and tetrahedrite. The origin of these nanoparticles can be related to processes already reported in the literature: (1) direct precipitation from the hydrothermal fluid or polymetallic melts entrained in them contemporaneously or after pyrite formation, and (2) exsolution of certain amounts of trace elements initially dissolved in the pyrite structure. In contrast, Co-Ni enrichment in porous zones of euhedral pyrite collected from the stockwork mineralization is related with irregular distribution of nano-sized domains of arsenian pyrite and/or arsenopyrite in As-free pyrite. This type of pyrite contains Au-Ag-Hg inclusions consisting of crystalline nanodomains and NPs of Au^0/Ag^0 or electrum, whose origin may be mainly related with precious metals mobilized along with semimetals like Hg or Bi by hydrothermal fluids or melts that circulated during stockwork formation or afterwards during regional metamorphism at higher temperatures in the range of 350–380 °C. Finally, our nanoscale study indicate that the relatively high concentrations of the trace metals measured by EMPA and LA-ICP-MS in pyrite from the IPB need to be reconsidered, owing the fact that these pyrite grains may contain abundant metal-based NPs. On a more positive note, the identification of NPs in pyrite grains from VMS deposits of the IPB can give a wider

perspective on the sources and evolution of the these economically interesting deposits.

Declaration of Competing Interest

The authors declare that they have no known competing financial interests or personal relationships that could have appeared to influence the work reported in this paper.

Acknowledgements

The Spanish project CGL2016-79204-R provided funding for field emission gun–environmental scanning electron microscopy (FEG-ESEM) and electron microprobe microanalyses (EMPA)/laser ablation–inductively coupled plasma–mass spectrometry (LA-ICP-MS) analyses of sulfides, respectively, while the PID2019-111715 GB-I00 and 18/IF/6347 project financed FIB-HRTEM analyses. Research grants, infrastructures, and human resources leading to this research have benefited from funding by the European Social Fund and the European Regional Development Fund. Laura Casado (LMA, Instituto de Nanociencia de Aragón (INA) – University of Zaragoza), María del Mar Abad and Cecilia de la Prada (CIC, University of Granada) are acknowledged for her assistance with FIB and HRTEM respectively. We are also indebted to Cristóbal Cantero from University of Huelva or their careful help with EMPA.

Funding for open access charge

Universidad de Granada / CBUA I was required by my former university to include that in order to keep the possibility of publishing the paper in open access.

Appendix A. Supplementary data

Supplementary data to this article can be found online at https://doi.org/10.1016/j.oregeorev.2022.104875.

References

Abraitis, P.K., Pattrick, R.A.D., Vaughan, D.J., 2004. Variations in the compositional and electrical properties of natural pyrite: a review. Int. J. Mineral Processing 74, 41–59.

Almodóvar, G.R., Sáez, R., Pons, J.M., Maestre, A., Toscano, M., Pascual, E., 1998. Geology and genesis of the Aznalcóllar massive sulphide deposits, Iberian Pyrite Belt. Spain. Miner. Depos. 33, 111–136.

Almodóvar, G.R., Yesares, L., Sáez, R., Toscano, M., González, F., Pons, J.M., 2019. Massive sulfide ores in the Iberian Pyrite Belt: mineralogical and textural evolution. Minerals 9, 653. https://doi.org/10.3390/min9110653.

Baurier, S., Jiménez-Franco, A., Roqué-Rosell, J., González-Jiménez, J.M., Gervilla, F., Proenza, J.A., Mendoza, J., Nieto, F., 2019. Nanoscale structure of zoned laurite from the Ojén ultramafic massif, southern Spain. Minerals 9, 288. https://doi.org/10.3390/min9050288.

Bayliss, P., 1977. Crystal structure refinement of a weakly anisotropic pyrite. Am. Mineral. 62, 1168–1172.

Becker, U., Reich, M., and Biswas, S., 2010. Nanoparticle–host interactions in natural systems. In F. Brenker, and G. Jordan, Eds., Nanoscopic Approaches in Earth and Planetary Sciences: EMU Notes in Mineralogy, 8, 1–52.

Bindi, L., Moelo, Y., Leone, P., Suchaud, M., 2012. Stoichiometric arsenopyrite, FeAsS, from La Roche-Balue Quarry, Loire-Atlantique, France: Crystal structure and Mossbauer study. Can. Mineral. 50, 471–479.

Bindi, L., Keutsch, F., Lepore, G.O., 2018. Structural and chemical study of weishanite, (Au, Ag, Hg), from the Keystone mine, Colorado, USA. Mineral. Mag. 82, 1141–1145.

Blanchard, M., Wright, K., Catlow, R.A., 2007. Arsenic incorporation into FeS_2 pyrite and its influence on dissolution: a DFT study. Geochim. Cosmochim. Acta 71, 624–630.

Buffat, P., Borrel, J.P., 1976. Size effect on the melting temperature of Au particles. Phys. Rev. A13, 2287–2298.

Burda, C., Chen, X., Narayanan, R., El-Sayed, M.A., 2005. Chemistry and properties of nanocrystals of different shapes. Chem. Rev. 105, 1025–1102. https://doi.org/10.1021/cr030063a.

Burke, M., Rakovan, J., Krekeler, M.P.S., 2017. A study by electron microscopy of gold and associated minerals from Round Mountain, Nevada. Ore Geol. Rev. 91, 708–717.

Castro, T., Reifenberger, R., Choi, E., Andres, R.P., 1990. Size-dependent melting temperature of individual nanometer-sized metallic clusters. Phys. Rev. B 42, 8548. https://doi.org/10.1103/PhysRevB.42.8548.

Castroviejo, R., Quesada, C., Soler, M., 2011. Post-depositional tectonic modification of VMS deposits in Iberia and its economic significance. Miner. Depos. 46, 615–1537.

Cepedal, A., Fuertes-Fuente, M., Martín-Izard, A., González-Nistal, S., Rodríguez-Pevida, L., 2006. Tellurides, selenides and Bi-mineral assemblages from the Río Narcea Gold Belt, Asturias, Spain: genetic implications in Cu–Au and Au skarns. Mineral. Petrol. 87, 277–304. https://doi.org/10.1007/s00710-006-0127-7.

Chang, L.L.Y., Bever, J.E., 1973. Lead sulfosalts minerals: crystal structures, stability relations, and paragenesis. Minerals Sci. Eng. 5, 181–191.

Ciobanu, C.L., Cook, N.J., Pring, A., 2005. Bismuth tellurides as gold scavengers. In: Mao, J.W., Bierlein, F.P. (Eds.), Mineral Deposit Research: Meeting the Global Challenge. Springer, Berlin, Heidelberg, New York, pp. 1387–1390.

Ciobanu, C., Birch, W.D., Cook, N.J., Pring, A., Grundler, P.V., 2010. Petrogenetic significance of Au–Bi–Te–S associations: the example of Maldon, Central Victorian gold province, Australia. Lithos 116, 1–17.

Ciobanu, C.L., Cook, N.J., Utsonomiya, S., Pring, A., Green, L., 2011. Focussed ion beam-transmission electron microscopy applications in ore mineralogy: Bridging micro- and nanoscale observations. Ore Geol. Rev. 42, 6–31.

Ciobanu, C.L., Cook, N.J., Utsonomiya, S., Kogagwa, M., Green, L., Gilbert, S., Wade, B., 2012. Gold-telluride nanoparticles revealed in arsenic-free pyrite. Am. Mineral. 97, 1515–1618.

Cölfen, H., Antonietti, M., 2005. Mesocrystals: Inorganic Superstructures Made by Highly Parallel Crystallization and Controlled Alignment. Angew. Chem. Int. Ed. 44, 5576–5591.

Cook, N.J., Ciobanu, C.L., 2004. Bismuth tellurides and sulphosalts from the Larga hydrothermal system, Metaliferi Mts., Romania: paragenesis and genetic significance. Mieneral. Mag., 68, 301–321.ç.

Cook, N.J., Ciobanu, C.L., Mao, J., 2009. Textural controls on gold distribution in As-free pyrite from the Dongping, Huangtuliang and Hougou gold deposits, North China Craton (Hebei Province, China). Chem. Geol. 264, 101–121.

Craig, J.R., Chang, L.L.Y., Lers, W.R., 1973. Investigations in the Pb-Sb-S system. Can. Mineral. 12, 199–206.

Davey, W.P., 1925. Lattice constants of twelve common metals. Phys. Rev. 25, 753–761.

De Yoreo, J.J., Gilbert, P.U., Sommerdijk, N.A., et al. (12 more authors) (2015) Crystallization by particle attachment in synthetic, biogenic, and geologic environments. Science, 349 (6247). aaa6760. ISSN 0036-8075.

Deditius, A.P., Utsunomiya, S., Renock, D., Ewing, R.C., Ramana, C.V., Becker, U., Kesler, S.E., 2008. A proposed new type of arsenian pyrite: composition, nanostructure and geological significance. Geochim. Cosmochim. Acta 72, 2919–2933.

Deditius, A.P., Utsunomiya, S., Reich, M., Kesler, S.E., Ewing, R.C., Hough, R., Walshe, J., 2011. Trace metal nanoparticles in pyrite. Ore Geol. Rev. 42, 32–46.

Deditius, A.P., Reich, M., Kesler, S.E., Utsunomiya, S., Chryssoulis, S.L., Walshe, J., Ewing, R.C., 2014. The coupled geochemistry of Au and As in pyrite from hydrothermal ore deposits. Geochim. Cosmochim. Acta 140, 644–670.

Douglas, N., 2000. The liquid bismuth collector model: an alternative gold deposition mechanism. In: Geological Society of Australia Abstracts. Geological Society of Australia. vol. 1999. pp. 135.

Fang, J., Ding, B., Gleiter, H., 2011. Mesocrystals: syntheses in metals and applications. Chem. Soc. Rev. 40, 5347–5360.

Farrow, C.F.G., Watkinson, D.H., 1992. Alteration and the role of fluids in Ni, Cu, and platinum-group element deposition, sudbury igneous complex contact, Onaping-Levack area. Ontario. Mineral. Petrol. 46, 67–83.

Fleet, M.E., Mumin, A.H., 1997. Gold-bearing arsenian pyrite and marcasite and arsenopyrite from Carlin Trend gold deposits and laboratory synthesis. Am. Mineral. 821–2, 182–193. https://doi.org/10.2138/am-1997-1-220.

Fleet, M.E., MacLean, P.J., Barbier, J., 1989. Oscillatory-zoned As-bearing pyrite from strata-bound and stratiform gold deposits; an indicator of ore fluid evolution. Econ. Geol. Monog. 6, 356–362.

Foit, F.F., Hughes, J.M., 2004. Structural variations in mercurian tetrahedrite. Sample A2 from the Spring Creek Claims in Harney County. Oregon. Am. Mineral. 89, 159–163.

Fougerouse, D., Micklethwaite, S., Tomkins, A.G., Mei, Y., Kilburn, M., Guadliardo, P., Fisher, L.A., Halfpenny, A., Gee, M., Paterson, D., Howard, D.L., 2016. Gold remobilization and formation of high-grade ore shoots driven by dissolution-reprecipitation replacement and Ni substitution into auriferous arsenopyrite. Geochim. Cosmochim. Acta 178, 143–159.

Fougerouse, D., Reddy, S.M., Aylmore, M., Yang, L., Guagliardo, P., Saxey, D.W., Rickard, W.D.A., Timms, N., 2021. A new kind of invisible gold in pyrite hosted in deformation-related dislocations. Geology 49. https://doi.org/10.1130/G49028.1.

Frens, G., 1973. Controlled Nucleation for the Regulation of the Particle Size in Monodisperse Gold Suspensions. Nature Physical Science 241, 20–22. https://doi.org/10.1038/physci241020a0.

Frost, B.R., Mavrogenes, J.A., Tomkins, A., 2002. Partial melting of sulfide ore deposits during medium- and high-grade metamorphism. Can. Mineral. 40, 1–18. https://doi.org/10.2113/gscanmin.40.1.1.

Gartman, A., Hannington, M., Jamieson, J.W., Peterkin, B., Garbe-Schönberg, D., Findlay, A.J., Fuchs, S., Kwasnitschka, T., 2018. Boiling-induced formation of colloidal gold in black smoker hydrothermal fluid. Geology 46, 39–42. https://doi.org/10.1130/G39492.1.

Genna, D., Gaboury, D., 2015. Deciphering the hydrothermal evolution of a VMS system by LA-ICP-MS using trace elements in pyrite: An example from the Bracemac-McLeod deposits, Abitibi, Canada, and implications for exploration. Econ. Geol. 110, 2087–2108.

González-Jiménez, J.M., Reich, M., 2017. An overview of the platinum- group element nanoparticles in mantle-hosted chromite deposits. Ore Geol. Rev. 8, 1236–1248.

González-Jiménez, J.M., Deditius, A., Gervilla, F., Reich, M., Suvorova, A., Roberts, M.P., Roqué, J., Proenza, J.A., 2018. Nanoscale partitioning of Ru, Ir, and Pt in base-metal sulfides from the Caridad chromite deposit. Cuba. Am. Mineral. 103, 1208–1220.

González-Jiménez, J.M., Piña, R., Kerestedjian, T.N., Gervilla, F., Borrajo, I., Farré-de-Pablo, J., Proenza, J.A., Tornos, F., Roqué, J., Nieto, F., 2021. Mechanisms for Pd-Au enrichment in porphyry-epithermal ores of the Elatsite deposit. Bulgaria. J. Geoch. Explor. 220, 106664 https://doi.org/10.1016/j.gexplo.2020.106664.

Guimarães, F.S., Cabral, A.R., Lhemann, B., Rios, F.J., Vila, M.A.B., Paulo de Castro, M., Queiroga, G.N., 2019. Bismuth-Melt Trails Trapped in Cassiterite–Quartz Veins. https://doi.org/10.1111/ter.12391.

Hall, H.T., Yund, R.A., 1964. Equilibrium relations among some silver sulfosalts and arsenic sulfides (abst.) Amer. Geophys. Union Trans. 45, 122.

Hannington, M., Hardardóttir, V., Garbe-Schonberg, D., Brown, K., 2016. Gold enrichment in active geothermal systems by accumulating colloidal suspensions. Nat. Geosci. 9 (4), 299–302.

Hannington, M., Garbe-Schöngerb, D., 2019. Detection of gold nanoparticles in hydrothermal fluids. Econ. Geol. 114, 397–400. https://doi.org/10.5382/econgeo.2019.4636.

Harrichhausen, N.J., 2016. Role of colloidal transport in the formation of high-grade gold veins at Brucejack, British Columbia. Ph. D. Thesis, Montréal, 137 pp.

Hastie, E.C.G., Schindler, M., Kontak, D.J., Lafrance, B., 2021. Transport and coarsening of gold nanoparticles in an orogenic deposit by dissolution–reprecipitation and Ostwald ripening. Commun Earth Environ 2, 57. https://doi.org/10.1038/s43247-021-00126-6.

Herrington, R.J., Wilkinson, J.J., 1993. Colloidal gold and silica in mesothermal vein systems. Geology 21, 539–542.

Hochella Jr., M.F., Lower, S.K., Maurice, P.A., Penn, R.L., Sahai, N., Sparks, D.L., Twining, B.S., 2008. Nanominerals, mineral nanoparticles, and Earth systems. Science 319, 1631–1638.

Hough, R.M., Noble, R.R.P., Reich, M., 2011. Natural gold nanoparticles. Ore Geol. Rev. 42, 55–61. https://doi.org/10.1016/j.oregeorev.2011.07.003.

Huston, D.L., Large, R.R., 1989. A chemical model for the concentration of gold in volcanogenic massive sulphide deposits. Ore Geol. Rev. 4, 171–200.

Ishida, M., Romero, R., Leisen, M., Yasukawa, K., Nakamura, K., Barra, F., Reich, M., Kato, Y., 2021. Auriferous pyrite formed by episodic fluid inputs in the Akeshi and Kasuga high-sulfidation deposits, Southern Kyushu. Japan. Miner. Depos. 57, 129–145. https://doi.org/10.1007/s00126-021-01053-4.

Jette, E.R., Foote, F., 1935. Precision determination of lattice constants. J. Chem. Phys. 3, 605–616.

Jian, W., Mao, J.W., Lehmann, B., Cook, N.J., Xie, G.Q., Liu, P., Duan, C., Alles, J., Niu, Z. J., 2021. Au-Ag-Te-rich melt inclusions in hydrothermal gold-quartz veins, Xiaoqinling lode gold district, central China. Econ. Geol. 116, 1239–1248.

Jian, W., Mao, J., Cook, N.J., Chen, L., Xie, G., Xu, J., Song, S., Hao, J., Li, R., Liu, J., 2022. Intracrystalline migration of polymetallic Au-rich melts in multistage hydothermal systems: example from the Xiaoqinling lode gold district, central China. Miner. Depos. https://doi.org/10.1007/s00126-021-01090-z.

Jiménez-Franco, A., González-Jiménez, J.M., Roqué, J., Proenza, J.A., Gervilla, F., Nieto, F., 2020. Nanoscale constraints on the in situ transformation of Ru-Os-Ir sulfides to alloys at low temperature. Ore Geol. Rev. 124, 103640 https://doi.org/10.1016/j.oregeorev.2020.103640.

Junge, M., Wirth, R., Oberthür, R., Melcher, F., Schreiber, A., 2015. Mineralogical siting of platinum-group elements in pentlandite from the Bushveld Complex. South Africa. https://doi.org/10.1007/s00126-014-0561-0.

Kanellopoulos, C., Mitropoulos, P., Valsami-Jones, E., Voudouris, P., 2017. A new terrestrial active mineralizing hydrothermal system associated with ore-bearing travertines in Greece (northernEuboea Island and Sperchios area). J. Geochim. Explor. 179, 9–24. https://doi.org/10.1016/j.gexplo.2017.05.003.

Keith, M., Häckel, F., Haase, K.M., Schwarz-Schampera, U., Klemd, R., 2016. Trace element systematics of pyrite from submarine hydrothermal vents. Ore Geol. Rev. 72, 728–745.

Kesler, S.E., Deditius, A.P., Reich, M.M., Utsunomiya, S., Ewing, R.C., 2010. Role of arsenian pyrite in hydrothermal ore deposits: a history and update. Geological Society of Nevada Symposium, May 14–22.

Lee, J., Yang, J., Kwon, S.G., Hyeon, T., 2016. Nonclassical nucleation and growth of inorganic nanoparticles. Nat. Rev. https://doi.org/10.1038/natrevmats.2016.34, 1 article 16034.

Leistel, J., Marcoux, E., Thiéblemont, Q., C., Sánchez, A., Almodóvar, G.R., Pascual, E., Sáez., 1998. The volcanic-hosted massive sulphide deposits of the Iberian Pyrite Belt Review and preface to the Thematic Issue. Mineral. Depos 33, 2–30. https://doi.org/10.1007/s001260050130.

Li, D., Nielsen, M.H., Lee, J.R.I., Frandsen, C., Banfield, J.F., De Yoreo, J.J., 2012. Direction-Specific Interactions Control Crystal Growth by Oriented Attachment. Science 336 (6084), 1014–1018. https://doi.org/10.1126/science.1219643.

Liu, W., Chen, M., Yang, Y., Mei, Y., Etschmann, B., Brugger, J., Johannessen, B., 2019. Colloidal gold in sulphur and citrate-bearing hydrothermal fluids: An experimental study. Ore Geol. Rev. 114, 103142 https://doi.org/10.1016/j.oregeorev.2019.103142.

Marcoux, E., Moëlo, Y., Leistel, J.M., 1996. Bismuth and cobalt minerals: indicators of stringer zones to massive sulfide deposits, Iberian Pyrite Belt. Miner. Depos. 31, 1–26. https://doi.org/10.1007/BF00225392.

Marignac, C., Diagana, B., Cathelineau, M., Boiron, M.-C., Banks, D., Fourcade, S., Jean Vallance, J., 2003. Remobilisation of base metals and gold by Variscan metamorphic fluids in the south Iberian pyrite belt: evidence from the Tharsis VMS deposit. Chem. Geol. 194, 143–165.

Maske, S., Skinner, B.J., 1971. Studies of the sulfosalts of copper I. Phases and phase relations in the system Cu-As-S. Econ. Geol. 66, 901–918.

Massalki, T.B., 1957. The lattice spacings of close-packed hexagonal Au-In, Au-Cd, and Au-Hg alloys. Acta Metall. 5, 541–547.

McCoy, D.T., 2000. Mid-Cretaceous Plutonic-Related Gold Deposits of Interior Alaska: Metallogenesis, Characteristics, Gold Associative Mineralogy and Geochronology. University of Alaska, Fairbanks, p. 245 p. [Ph.D. Thesis].

McFall, K.A., Naden, J., Roberts, S., Baker, T., Spratt, J., McDonald, I., 2018. Platinum-group minerals in the Skouries Cu-Au (Pd, Pt, Te) porphyry deposit. Ore Geol. Rev. 99, 344–364.

McLeish, D.F., Williams-Jones, A.E., Vasyukova, O.V., Clarck, J.R., Board, W.S., 2021. Colloidal transport and flocculation are the cause of the hyperenrichment of gold in nature. PNAS 118 (20), e2100689118. https://doi.org/10.1073/pnas.2100689118.

McMclenaghan, S.H., Lentz, D.R., Cabri, L.J., 2004. Abundance and speciation of gold in massive sulfides of the Bathurst mining camp, New Brunswick. Canada. Can. Mineral. 42, 851–871.

Merkulova, M., Mathon, O., Glatzel, P., Rovezzi, M., Batanova, V., Marion, P., Boiron, M.-C., Manceau, A., 2019. Revealing the chemical form of "invisible" gold in natural arsenian pyrite and arsenopyrite with high Energy-Resolution X-ray Absorption Spectroscopy. ACS Earth Space Chem. 3 (9), 1905–1914. https://doi.org/10.1021/acsearthspacechem.9b00099.hal-02314773.

Morishita, Y., Hammond, N.Q., Momii, K., Konagaya, R., Sano, Y., Takahata, N., Ueno, H., 2019. Invisible Gold in Pyrite from Epithermal, Banded-Iron-Formation-Hosted, and Sedimentary Gold Deposits: Evidence of Hydrothermal Influence. Minerals 9, 447.

Nehlig, P., Cassard, D., Marcoux, E., 1998. Geometry and genesis of feeder zones of massive sulphide deposits: constraints from the Rio Tinto ore deposit (Spain). Miner. Depos. 33, 137–149.

Nocete, F., Álex, E., Nieto, J.M., Sáez, R., Bayona, M.R., 2005. An archaeological approach to regional environmental pollution in the southwestern Iberian Peninsula related to third millennium BC mining and metallurgy. J. Archaeol. Sci. 32, 1566–1576. https://doi.org/10.1016/j. jas.2005.04.012.

Noda, Y., Masumoto, K., Ohba, S., Saito, Y., Toriumi, K., Iwata, Y., Shibuya, I., 1987. Temperature dependence of atomic thermal parameters of lead chalcogenides, PbS, PbSe and PbTe. Acta Crystallogr. A C43, 1443–1445.

Novgorodova, M.I., Gorshkov, A.I., Mokhov, A.V., 1981. Native silver and its new structural modifications. Int. Geol. Rev. 23, 485–494.

Palenik, C.S., Ustunomiya, S., Reich, M., Kesler, S.E., Wang, L., Ewing, R.C., 2004. "Invisible" gold revealed: direct imagining of gold nanoparticles in a Carlin-type deposit. Am. Mineral. 89, 1359–1366.

Pals, D.W., Spry, P.G., Chryssoulis, S., 2003. Invisible gold and tellurium in arsenic-rich pyrite from the Emperor gold deposit, Fiji: implications for gold distribution and deposition. Econ. Geol. 98, 479–493.

Paton, C., Hellstrom, J., Paul, B., Woodhead, J., Hergt, J., 2011. Iolite: freeware for the visualisation and processing of mass spectrometric data. J. Anal. At. Spectrom. VL -IS. https://doi.org/10.1039/C1JA10172B. online.

Peterson, R.C., Miller, I., 1986. Crystal structure and cation distribution in freibergite and tetrahedrite. Mineral. Mag. 50, 717–721.

Petrella, L., Thebaud, N., Fougerouse, D., Martin, L., Turner, S., Suvorova, A., Gain, S., 2021. Crustal-scale transport of nanoparticle emulsion forms ore deposits. Research Square. https://doi.org/10.21203/rs.3.rs-669530/v1.

Pinedo Vara, I., 1963. Las piritas de Huelva. Su historia, minería y aprovechamiento. Summa, Madrid, 1.003 pp.

Piña, R., Gervilla, F., Barnes, S.-J., Ortega, L., Lunar, R., 2012. Distribution of platinum-group and chalcophile elements in the Aguablanca Ni-Cu sulfide deposit (SW Spain): evidence from a LA-ICP-MS study. Chem. Geol. 302–303, 61–75. https://doi.org/10.1016/j.chemgeo.2011.02.010.

Polte, J., 2015. Fundamental growth principles of colloidal metal nanoparticles – a new perspective. Cryst. Eng. Comm. 17, 6809–6830. https://doi.org/10.1039/C5CE01014D.

Prokofiev, V.Y., Banks, D.A., Lobanov, K.V. et al. Exceptional Concentrations of Gold Nanoparticles in 1,7 Ga Fluid Inclusions From the Kola Superdeep Borehole, Northwest Russia. Sci Rep 10, 1108. https://doi.org/10.1038/s41598-020-58020-8.

Putnis, A., 2002. Mineral replacement reactions: from macroscopic observations to microscopic mechanisms. Min. Mag. 66, 689–708.

Qian, G., Brugger, J., Testemale, D., Skinner, W., Pring, A., 2013. Formation of As(II)-pyrite during experimental replacement of magnetite under hydrothermal conditions. Geochim. Cosmochim. Acta 100, 1–10. https://doi.org/10.1016/j.gca.2012.09.034.

Rieder, M., Crelling, J.C., Sustai, O., Drabek, M., Weiss, Z., Klementova, M., 2007. Arsenic in iron disulfides in a brown coal from the North Bohemian Basin. Czech Republic. Int. J. Coal Geology 71, 115–121.

Reich, M., Becker, U., 2006. First-principles calculations of the thermodynamic mixing properties of arsenic incorporation into pyrite and marcasite. Chem. Geol. 225, 278–290.

Reich, M., Kesler, S.E., Utsunomiya, S., Palenik, C.S., Chryssoulis, S.L., Ewing, R.C., 2005. Solubility of gold in arsenian pyrite. Geochim. Cosmochim. Acta 69, 2781–2796.

Reich, M., Utsunomiya, S., Kesler, S.E., Wang, L.M., Ewing, R.C., Becker, U., 2006. Thermal behaviour of metal nanoparticles in geologic materials. Geology 34, 1033–1036.

Reich, M., Deditius, A., Chryssoulis, S., Li, J.-W., Ma, C.-Q., Parada, M.A., Barra, F., Mittermayr, F., 2013. Pyrite as a record of hydrothermal fluid evolution in porphyry copper system: a SIMS/EMPA trace element study. Geochim. Cosmochim. Acta 104, 42–62.

Relvas, J.M.R.S., Tassinari, C.G., Munhá, J., Barriga, F.J.A.S., 2001. Multiple sources for ore-forming fluids in the Neves Corvo VMS deposit of the Iberian Pyrite belt (Portugal): strontium, neodymium and lead isotope evidence. Miner Depos 36, 416–427.

Ruiz, C., Arribas, A., Arribas, A., Jr, B., 2002. Mineralogy and geochemistry of the Masa Valverde blind massive sulphide deposit, Iberian Pyrite Belt (Spain). Ore Geol. Rev. 19, 1–22. https://doi.org/10.1016/S0169-1368(01)00037-3.

Sáez, R., Pascual, E., Toscano, M., Almodóvar, G.R., 1999. The Iberian type of volcano-sedimentary massive sulphide deposits. Miner. Depos. 34, 549–570.

Saéz, R., 2010. La Faja Pirítica Ibérica. Una Perspectiva Geológica, Arqueológica y Ambiental. University of Huelva, Huelva, Spain. Unpublished. Ph.D. Thesis.

Sánchez-Ramírez, J.F., Pal, U., Nolasco-Hernández, L., Mendoza-Álvarez, J., Pescador-Rojas, J.A., 2008. Synthesis and optical properties of Au-Ag alloy nanoclusters with controlled composition. Journal of Nanomaterials. Article ID 620412. https://doi.org/10.1155/2008/620412.

Saunders, J.A., 1990. Colloidal transport of gold and silica in epithermal precious metal systems: evidence from the Sleeper deposit, Humboldt County, Nevada. Geology 18, 757–760.

Saunders, J.A., Burke, M., 2017. Formation and Aggregation of Gold (Electrum) Nanoparticles in Epithermal Ores. Minerals 7, 163. https://doi.org/10.3390/min7090163.

Saunders, J.A., Burke, M., Brueseke, M.E., 2020. Scanning-electron-microscope imaging of gold (electrum) nanoparticles in middle Miocene bonanza epithermal ores from northern Nevada. USA. Miner. Depos. 55, 389–398. https://doi.org/10.1007/s00126-019-00935-y.

Seward T. M., Williams-Jones A. E., Migdisov A. A., 2014. The chemistry of metal transport and deposition by ore-forming hydrothermal fluids. In Treatise on Geochemistry (eds. K. Turekian and H. Holland). 2nd edition. V. 13. Elsevier, pp. 29-57.

Simon, G., Huang, H., Penner-Hahn, J.E., Kesler, S.E., Kao, L.-S., 1999. Oxidation state of gold and arsenic in gold-bearing arsenian pyrite. Am. Mineral. 84, 1071–1079.

Sung, Y.-H., Brugger, J., Ciobanu, C.L., Pring, A., Skinner, W., Nugus, M., 2009. Invisible gold in arsenian pyrite and arsenopyrite from a multistage Archean gold deposit: Sunrise Dam Eastern Goldfields Province, Western Australia. Miner. Deposita 44, 765–791.

Toermanen, T.O., Koski, R.A., 2005. Gold enrichment and the Bi-Au association in pyrrhotite- rich massive sulfide deposits, Escanaba Trough, Southern Gorda Ridge. Econ. Geol. Bull. Soc. Econ. Geol. 100, 1135–1150.

Tooth, B., Brugger, J., Ciobanu, C., Liu, W., 2008. Modeling of gold scavenging by bismuth melts coexisting with hydrothermal fluids. Geology 36, 815–818. https://doi.org/10.1130/G25093A.1.

Tooth, B., Ciobanu, C.L., Green, L., O'Neill, B., Brugger, J., 2011. Bi-melt formation and gold scavenging from hydrothermal fluids: an experimental study. Geochim. Cosmochim. Acta 75 (2011), 5423–5443.

Torró, L., Benites, D., Vallance, J., Laurent, O., Ortiz-Benavente, B.A., Chelle-Michou, C., Proenza, J.A., Fontboté, L., 2022. Trace element geochemistry of sphalerite and chalcopyrite in arc-hosted VMS deposits. J. Geochim. Explor. 232, 106882.

Tornos, F., 2006. Environment of formation and styles of volcanogenic massive sulfides: the Iberian pyrite belt. Ore Geol. Rev. 28, 259–307.

Wang, F., Richards, V.N., Shields, S.P., Buhro, W.E., 2014. Kinetics and mechanisms of aggregative nanocrystal growth. Chem. Mater. 26, 5–21.

Watari, T., Nansi, K., Nakajima, K., 2020. Review of critical metal dynamics to 2050 for 48 elements. Resour. Conserv. Recycl. 155, 104669 https://doi.org/10.1016/j.resconrec.2019.104669.

Weitz, D.A., Huang, J.S., 1984. Self-similar structures and the kinetics of aggregation of gold colloids. In: Family, F., Landau, D.P. (Eds.), Kinetics of aggregation and gelation. Elsevier, New York, pp. 19–27.

Wells, A.F., 1984. Structural Inorganic Chemistry, 5 th Edition. Clarendon Press, Oxford. [p. 1288, "Metallic radii for 12-coordination"].

Wirth, R., Reid, D., Schreiber, A., 2013. Nanometer-sized platinum-group minerals (PGM) in base metal sulfides: new evidence for an orthomagmatic origin of the Merensky reef PGE ore deposit Bushveld Complex. South Africa. Can. Mineral. 51, 143–155.

Wright, J., Lentz, D.R., Rossiter, S., Garland, P., 2016. Analysis of Au-Ag Mineralization in the Caribou Base-Metal VMS Deposit, New Brunswick: Examination of Micro-Scale Inter- and Intra-Sulphide Distribution and Its Relation to Geometallurgy. Minerals 6, 113.

Wyckoff, R.W.G., 1963. Cubic closest packed, ccp, structure. Crystal Structures 1, 7-83 Second edition. Interscience Publishers, New York, New York.

Xia, F., Brügger, J., Chen, G., Ngothai, Y., O'Neill, B., Putnis, A., Pring, A., 2009. Mechanism and kinetics of pseudomorphic mineral replacement reactions: a case study of the replacement of pentlandite by violarite. Geochim. Cosmochim. Acta 73, 1945–1969.

Xing, Y., Brugger, J., Tomkins, A., Shvarov, Y., 2019. Arsenic evolution as tool for understanding formation of pyritic gold ores. Geology 47, 335–338, 10.1130/G45708.1.

Xiong, F., Zoheir, B., Wirth, R., Milushi, I., Qiu, T., Yang, J., 2021. Mineralogical and isotopic peculiarities of high-Cr chromitites: implications for a mantle convection genesis of the Bulqiza ophiolite. Lithos 398–399. https://doi.org/10.1016/j.lithos.2021.106305.

Yesares, L., Sáez, R., Almodóvar, G.R., Nieto, J.M., Gómez, C., Ovejero, G., 2017. Mineralogical evolution of the Las Cruces gossan cap (Iberian Pyrite Belt): from subaerial to underground conditions. Ore Geol. Rev. 80, 377–405.

Zhang, Y., Zhen, S., Wang, D., Liu, J., Wang, J., Zha, Z., Bai, H., 2021. In situ trace elements and sulfur isotopes of sulfides in the Dabaiyang Te-Au deposit, Hebei Province, China: Implications for Au remobilization from pyrite. Ore Geol. Rev. 140, 104626 https://doi.org/10.1016/j.oregeorev.2021.104626.

Zhou, L., O'Brien, P., 2012. Mesocrystals — properties and applications. J. Phys. Chem. Lett. 3, 620–628.

Zhou, H., Sun, X., Cook, N.J., Lin, H., Fu, Y., Zhong, R., Brügger, J., 2017. Nano- to micron-scale particulate gold hosted by magnetite: a product of gold scavenging by bismuth melts. Econ. Geol. 112, 993–1010.

Zhou, H., Wirth, R., Gleeson, S.A., Mayanna, S., 2021. Three-dimensional and microstructural fingerprinting of gold nanoparticles at fluid-mineral interfaces. Am. Mineral. 106, 97–104. https://doi.org/10.2138/am-2021-7696.